On the Ungerboeck and Forney Observation Models for Spatial Combining And Their Application to 5G Millimeter-Wave Bands

FARAH ARABIAN, (Student Member, IEEE), GREGORY P. NORDIN, (Senior Member, IEEE), AND MICHAEL RICE [ID], (Fellow, IEEE)
Department of Electrical and Computer Engineering, Brigham Young University, Provo, UT 84602, USA
Corresponding author: Farah Arabian (farah.arabian@byu.edu)

ABSTRACT Equivalent discrete-time models for a variety of spatial combining techniques operating in a frequency-selective multipath fading channel are derived. The equivalent discrete-time models are used to perform computer simulations of the post-equalizer bit error rate over a frequency-selective multipath channel whose derivation preserved polarization state information. Two sets of computer simulations were performed. In the first set, the performance of co-located cross-polarized antenna elements was investigated. The results showed that maximum likelihood combining maximizes polarization diversity, but that maximum ratio combining and selection combining were very competitive in the case where the cross-polarized antennas produce one strong channel and a relatively weak channel. Elliptical combining, using a 90° hybrid coupler, produced the worst results. The second set of simulations used a combination of spatial and cross-polarized antenna elements, for a total of eight antenna elements. The simulation results showed that maximum likelihood combining was best, followed by maximum ratio combining, equal gain combining, and selection combining. Again, elliptical combining was the worst, leading to the conclusion that other combining techniques are preferred in frequency-selective fading environments.

INDEX TERMS Frequency-selective multipath fading, time-domain equalization, diversity combining, polarization diversity, 5G millimeter-wave band.

I. INTRODUCTION

To support high data-rate downlinks in 5G systems [1], wideband channels are required. In multipath environments, wideband channels exhibit frequency-selective fading. Equalization [2] is the most commonly applied technique to address the impact of frequency-selective fading. The realities of how mobile handsets are used motivate the use of multiple antennas in the mobile handset [3]. Consequently, the combination of spatial diversity reception and equalization is of interest and is the focus of this paper.

Spatial diversity can be realized in two ways: 1) the use of spatially-separated antennas by the receiver, and 2) the use of cross-polarized antenna elements. For example, the mobile handset antenna design described in [3] uses both. In both of its forms, spatial diversity presents to the detector multiple copies of the corrupted waveform generated

by the transmitter. The performance gains realized by spatial diversity depend on how uncorrelated the copies are [4].

Cross- (or dual-) polarized antennas have long been employed in mobile handsets to capture the received signal when the mobile is in an arbitrary orientation. Polarization diversity is an increasingly attractive source of spatial diversity in mobile handsets due to its ability to provide good antenna element isolation and to provide two outputs in a compact space through the use of co-located cross-polarized antenna elements [3]. The performance of polarization diversity reception depends on how uncorrelated the outputs of the two antenna elements are [5]–[8]. Reflections between the transmitter and receiver tend to decorrelate the outputs of the two antenna elements [6], but not completely [5]. Despite the lack of complete decorrelation, it is possible to realize performance gains using polarization diversity [6].

Optimal combining in a frequency-selective environment is a non-trivial problem. The traditional techniques, selection combining (SC), equal gain combining (EGC), and maximum ratio combining (MRC) have their origins in frequency

Notation	Description
I_n	the n-th symbol from a QAM alphabet of size M
$g(t)$	the unit-energy pulse shape used for the QAM signal
T_s	symbol time
$c(t)$	the complex-valued low-pass equivalent impulse response of the multipath channel
$C(f)$	the channel transfer function: the Fourier transform of $c(t)$
$z(t)$	the complex-valued low-pass equivalent additive thermal noise modeled as a circularly-symmetric normal random process
N_0	the parameter for the power spectral density level (with units W/Hz) of the additive thermal noise
$\star$	continuous-time linear convolution
$h(t)$	$= g(t) \star c(t)$, the distorted pulse shape observed at the channel output
$x(t)$	$h(t) \star h^*(-t)$, the correlation function of $h(t)$
$y(t)$	the output of a filter matched to $h(t)$
$\nu(t)$	the output of a filter matched to $h(t)$ due to the additive noise $z(t)$
UOM	the Ungerboeck observation model: an equivalent discrete-time system with input I_n, channel filter $x(nT_s)$, noise $\nu(nT_s)$, and output $y(nT_s)$
$X(z)$	the z-transform of $x(nT_s)$
FOM	the Forney observation model: a whitened version of the UOM based on the spectral factorization $X(z) = F(z)F^*(1/z^*)$. The input is I_k, the channel filter is f_k (the coefficient of z^{-k} in $F(z)$), the noise is $\eta(kT_s)$, and the output is $v(kT_s)$
XPD	cross polar discrimination
ρ_{env}	cross correlation of the signal envelope
ρ_{coh}	coherent cross correlation
$\mathcal{E}$	channel energy

non-selective fading channels [4]. The performance of the traditional techniques is well-understood in frequency non-selective fading channels but less well-understood in frequency selective fading channels. For co-located cross-polarized antenna elements, combining using a 90° hybrid coupler is a popular technique in microwave engineering. This is often termed "circular combining", but is more accurately called "elliptical combining" when the two signals being combined have different strengths. Scott [9] derived the optimum combiner in the maximum likelihood sense for frequency-selective fading channels. (Balaban [10] obtained the same result six years earlier via a minimum mean-squared error argument.)

The largest 5G bandwidth allocations exist in the millimeter wave (mmWave) band [11]. The multipath modeling and analysis performed in [12]–[18] confirm the frequency-selective nature of the fading and the need for equalization [19]. For this reason, the examples used in the paper focus on operation in the mmWave band at 28 GHz.

One of the greatest challenges of using the mmWave band for this application is the requirement of line-of-sight (LOS) propagation between the basestation and the mobile. This requirement has prompted the idea of a *network*-level approach to solving the problem. The concept assumes a dense population of basestations that allows a mobile to connect to multiple basestations. The idea is that a sufficiently dense deployment of basestations guarantees an LOS link

to at least one of the available basestations. A network-level analysis where multiuser interference is the dominant impairment was presented in [20]. A more recent publication [21] based on the same idea formulates the problem as a spatial diversity problem. Network-level performance is still a function of the link-level performance between a mobile and the available basestations. Consequently, the focus of this paper is on the underlying link-level system.

Modern radio systems implement equalization in the sampled data domain [2], [22]. Because the data are discrete and the equalizer operates in the discrete-time domain, the data-to-equalizer path may be abstracted using an equivalent discrete-time model. The equivalent discrete-time models of interest here are the Ungerboeck observation model [23] and the Forney observation model [24].

The main contribution of this paper is the development of the Ungerboeck and Forney observation models for the five combining techniques described above. We demonstrate the use of the Forney observation model in performing computer simulations to evaluate the post equalizer bit error rate for QPSK operating in a 5G urban environment in the mmWave band. To incorporate polarization state in the multipath channel model, a simple four-path multipath channel that preserves polarization state is developed. This represents a secondary contribution in the sense that it demonstrates how to include polarization state directly in a multipath propagation model without the need to *assume* values for the cross polar discrimination (XPD).

Given the popularity of multicarrier waveforms in 5G applications, a few comments on our use of a single carrier modulation are warranted. First, given the difficulties of producing linear RF power amplifiers with sufficient transmit power in the mmWave band, signals with low peak-to-average power ratio are preferred [25]. This is because low-peak-to-average power ratio signals reduce the output back-off required to achieve linear or near-linear performance. It is well known that single-carrier modulations have lower peak-to-average power ratios than multicarrier modulations. IEEE 802.11ad is a good example of a mmWave band communication system that uses a single-carrier modulation [26]. Second, in [27], it was shown that single-carrier modulations with time-domain equalization achieve superior performance, measured by achievable spectral efficiency and global energy efficiency, relative to single-carrier modulations with frequency-domain equalization and to MIMO-OFDM when the non-linear behavior of RF power amplifiers is included in the analysis. Third, single-carrier modulations have a performance advantage when operating over frequency-selective channels [28] in the sense that single-carrier modulations require no coding or high-rate codes in contrast to multicarrier modulations that require relatively power codes to achieve acceptable bit error rate performance. These three observations recommend single-carrier modulations as a *possibility* in mmWave systems. Initial results for multicarrier modulations with combining and equalization are presented by the authors in [29].
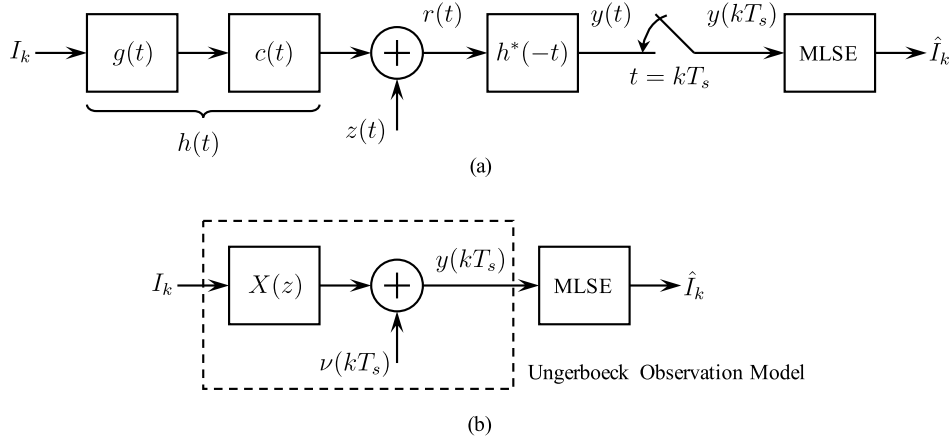
FIGURE 1. The ML detector for a linearly-modulated single-carrier modulation transmitted over a frequency-selective channel: (a) The sequence of steps used to produce the inputs to the ML sequence detector; (b) The equivalent discrete-time system—the Ungerboeck Observation Model.

This paper is organized as follows. A review of the Ungerboeck and Forney observation models is presented in Section II. In Section III, the Ungerboeck and Forney observation models are extended to the traditional combining techniques (SC, EGC, MRC, EPC) and to the maximum likelihood combiner. Numerical examples are presented in Section IV. The numerical examples are based on the downlink multipath channel derived in the Appendix where the massive-MIMO beamforming assumptions for the basestation transmitter are included in the analysis. The paper draws to a close with the conclusions presented in Section V.

II. THE UNGERBOECK AND FORNEY OBSERVATION MODELS

The original formulations of Ungerboeck [23] and Forney [24] observation models were based on a linearly-modulated single-carrier signal transmitted over a frequency-selective channel with impulse response $c(t)$. The received signal may be represented by its complex-valued low-pass equivalent waveform [2]

$$r(t) = \sum_{\ell} I_\ell g(t - \ell T_s) \star c(t) + z(t) \tag{1}$$

where I_ℓ is the ℓ-th symbol drawn from a QAM alphabet of size M, T_s is the symbol time, $g(t)$ is a unit energy pulse shape, $\star$ represents the continuous-time convolution operation, and $z(t)$ is the additive thermal noise modeled as a complex-valued circularly-symmetric normal random process with

$$E\{z(t + \tau)z^*(t)\} = 2N_0\delta(\tau) \tag{2}$$

where $\delta(\tau)$ is the Dirac impulse function. The maximum likelihood (ML) detector applies a filter matched to the received pulse $h(t) = g(t) \star c(t)$, samples the matched filter output every T_s seconds, and applies a sequence detector (the Viterbi Algorithm) to the sampled matched filter outputs. A block diagram summarizing this sequence of operations is shown

in Figure 1. The output of the matched filter is

$$y(t) = \sum_{\ell} I_\ell x(t - \ell T_s) + \nu(t) \tag{3}$$

where

$$x(t) = h(t) \star h^*(-t) \tag{4}$$

and $\nu(t)$ is a complex-valued circularly-symmetric normal random process with

$$E\{\nu(t + \tau)\nu^*(t)\} = 2N_0 x(\tau). \tag{5}$$

The sampled matched filter output is

$$y(kT_s) = \sum_{\ell} I_\ell x((k - \ell)T_s) + \nu(kT_s). \tag{6}$$

It is usually the case that $x(\ell T_s)$ is time-limited (or is well-approximated as such) so that $x(\ell T_s) = 0$ for $|\ell| > L$. Consequently, the sampled matched filter output (3) may be re-expressed as

$$y(kT_s) = \sum_{\ell=-L}^{L} I_{k-\ell} x(\ell T_s) + \nu(kT_s). \tag{7}$$

Equation (7) defines the finite state machine upon which the ML sequence detector operates. Exploiting the symmetries of the sampled correlation function $x(\ell T_s)$, the Viterbi Algorithm may be applied using the branch metrics

$$\lambda_k^{(\text{UOM})} = \text{Re}\left\{I_k^*\left(2y(kT_s) - I_k x(0) - 2\sum_{\ell=1}^{L} x(\ell T_s)I_{k-\ell}\right)\right\} \tag{8}$$

for the transition from state $I_{k-L}, \ldots, I_{k-1}$ to state $I_{k-L+1}, \ldots, I_k$.

Equation (7) also defines an equivalent discrete-time model that relates the samples $y(kT_s)$ to the transmitted symbols I_k. This equivalent discrete-time model is called *Ungerboeck Observation Model* and is illustrated in Figure 1 (b).
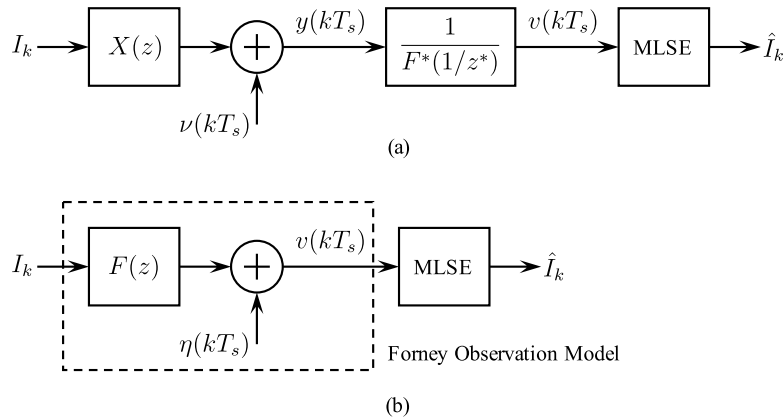
FIGURE 2. The ML detector for a linearly-modulated single-carrier modulation transmitted over a frequency-selective channel: (a) The sequence of steps used to produce the noise whitened model; (b) The equivalent discrete-time system—the Forney Observation Model.

The Ungerboeck observation model is often used in the case where its output, $y(kT_s)$ is applied to an equalizer instead of a sequence detector [2].

Because the correlation of the noise samples in (7) complicates both the application of the samples $y(kT_s)$ to the Viterbi Algorithm and the corresponding performance analysis, Forney [24] whitened the Ungerboeck observation model as follows. The power spectral density of the noise samples in (7) is [see (5)]

$$S_\nu(z) = 2N_0 X(z) \qquad (9)$$

where

$$X(z) = \sum_{\ell=-L}^{L} x(\ell T_s) z^{-\ell}. \qquad (10)$$

Because $x(\ell T_s)$ is a correlation function, the symmetry of the coefficients in the polynomial $X(z)$ produces $2L$ roots with L roots inside the unit circle and L roots outside the unit circle that are conjugate-reciprocals of the roots inside the unit circle. The whitening process begins with the spectral factorization

$$X(z) = F(z) F^*(1/z^*). \qquad (11)$$

Assigning all the roots inside the unit circle to $F(z)$, the noise whitening filter is $1/F^*(1/z^*)$, whose only stable inverse is a non-causal IIR system. The output of the noise whitening filter is a causal, stable FIR system with white noise. The steps are illustrated in Figure 2. In Figure 2, the output $v(kT_s)$ is

$$v(kT_s) = \sum_{\ell=0}^{L} f_\ell I_{k-\ell} + \eta(kT_s) \qquad (12)$$

where the channel coefficients $f_0, \ldots, f_L$ are defined by

$$F(z) = f_0 + f_1 z^{-1} + \cdots + f_L z^{-L} \qquad (13)$$

and $\eta(kT_s)$ is a complex-valued circularly symmetric normal random variable with

$$E\{\eta((k+m)T_s)\eta^*(kT_s)\} = 2N_0\delta_m \qquad (14)$$

where δ_m is the Kronecker delta. Equation (12) defines a finite state machine that is the foundation of the ML sequence detector. The Viterbi Algorithm may be applied using the branch metrics

$$\lambda_n^{\text{(FOM)}} = \left| v(nT_s) - \sum_{\ell=0}^{L} f_\ell I_{n-\ell} \right|^2 \qquad (15)$$

for the transition from from state $I_{n-L}, \ldots, I_{n-1}$ to state $I_{n-L+1}, \ldots, I_n$.

The equivalent discrete-time system defined by (12)–(14) is shown in Figure 2 (b). The equivalent discrete-time system is also known as the *Forney Observation Model*. Like the Ungerboeck observation model, the output $v(kT_s)$ may be applied to an equalizer instead of a sequence detector [2].

Historical Note—The presentation here leaves the reader with the impression that the Forney observation model was developed *after* the Ungerboeck observation model. This is not the case. Forney's work [24], published in 1972, obtained the Ungerboeck observation model as an intermediate step. Because the noise was correlated, Forney developed the noise whitening approach described above to produce a signal model with uncorrelated noise that was a natural fit to the Viterbi algorithm. Afterwards, Ungerboeck recognized that because the noise correlation and the ISI model are the same, the symmetries may be exploited to rewrite the log-likelihood function corresponding to (6) recursively, thus making it possible to apply the Viterbi algorithm using the branch metrics (8). This work was published by Ungerboeck two years after Forney in [23].

TABLE 2. A Summary of the Ungerboeck and Forney Observations Models for traditional combining techniques. In each row, $x(t) = h(t) \star h^*(-t)$, $h(t) = g(t) \star c(t)$. The last row only applies to two co-located cross-polarized antenna elements.

Combiner Method	$c(t)$	UOM noise PSD $S_\nu(z)$	FOM noise PSD $S_\eta(z)$
SC	$c_m(t)$	$2N_0 X_m(z)$	$2N_0$
EGC	$c_1(t) + \sum_{n=2}^{N} e^{j\phi_n} c_n(t)$	$N \times 2N_0 X_{EGC}(z)$	$N \times 2N_0$
MRC	$k_1 c_1(t) + \sum_{n=2}^{N} e^{j\phi_n} k_n c_n(t)$	$\left[\sum_{n=1}^{N} k_n^2\right] \times 2N_0 X_{MRC}(z)$	$\left[\sum_{n=1}^{N} k_n^2\right] \times 2N_0$
EPC	$c_1(t) \pm j c_2(t)$	$4N_0 X_{EPC}(z)$	$4N_0$

III. SPATIAL COMBINING TECHNIQUES AND THEIR UNGERBOECK AND FORNEY OBSERVATION MODELS

In this section we consider the case of N copies of the received signal produced by N spatially-separated antennas. The n-th copy of the signal is given by

$$r_n(t) = \sum_\ell I_\ell g(t - \ell T_s) \star c_n(t) + z_n(t) \qquad (16)$$

for $n = 1, \ldots, N$ where $c_n(t)$ is the impulse response of the propagation channel seen by the n-th antenna and $z_n(t)$ is a complex-valued circularly-symmetric normal random process with

$$E\{z_n(t+\tau) z_m^*(t)\} = \begin{cases} 2N_0 \delta(\tau), & n = m \\ 0, & n \neq m. \end{cases} \qquad (17)$$

Note that this noise model assumes that the thermal noise contribution accompanying each received signal has the same power spectral density and that the noise contributions accompanying the received signals from different antennas are uncorrelated.

Each channel is characterized by its energy

$$\mathcal{E}_n = \int_{-\infty}^{\infty} |c_n(t)|^2 dt \qquad (18)$$

for $n = 1, \ldots, N$. The channel energies are not normalized in order to preserve signal-to-noise advantages of strong channels over weak channels.

The combiner has, as its inputs, $r_n(t)$ for $n = 1, \ldots, N$ and outputs a single signal $r(t)$ formed from the combination of the N input signals. The traditional combining techniques are selection combining, equal gain combining, and maximum ratio combining. The Ungerboeck and Forney observation models for these techniques are described in Sections III-A–III-C. For the case of two co-located cross-polarized antenna elements, circular (or, more precisely, elliptical) combining is often used. The Ungerboeck and Forney observation models for elliptical combining are described in Section III-D. A summary of the results from Sections III-A – III-D is given in Table 2.

A. SELECTION COMBINING
In selection combining (SC), the combiner selects the "best" input signal as the combiner output. The definition of "best"

is straight-forward in the case of non-frequency selective fading (the "best" input is the strongest input). Motivated by the definition of "best" used for frequency non-selective channels, the output of a selection combiner for frequency-selective channels is

$$r(t) = r_m(t), \quad m = \underset{1 \leq n \leq N}{\arg\max} \{\mathcal{E}_n\}. \qquad (19)$$

The Ungerboeck observation model follows directly from (1) using $c(t) = c_m(t)$ and $z(t) = z_m(t)$. The Ungerboeck observation model is given by (7) and the Forney observation model by (12). These results are summarized in the second row of Table 2.

B. EQUAL GAIN COMBINING
In equal gain combining (EGC), the combiner co-phases and adds the received signals to produce the combiner output. Co-phasing is performed relative to a reference channel, which without loss of generality, is designated $r_1(t)$. The combiner output is

$$r(t) = r_1(t) + \sum_{n=2}^{N} e^{j\phi_n} r_n(t) \qquad (20)$$

$$= \sum_\ell I_\ell g(t - \ell T_s) \star \underbrace{\left[c_1(t) + \sum_{n=2}^{N} e^{j\phi_n} c_n(t) \right]}_{c_{\text{EGC}}(t)}$$

$$+ \underbrace{z_1(t) + \sum_{n=2}^{N} e^{j\phi_n} z_n(t)}_{z_{\text{EGC}}(t)} \qquad (21)$$

where ϕ_n is the phase shift required to co-phase $c_n(t)$ for $n = 2, \ldots, N$. In the case of non-frequency selective fading, the definition of the optimum phases is straight-forward. In the case of frequency-selective fading, the definition of optimum is less straight-forward. A reasonable definition of optimum is the phases that maximize the combined channel energy. (To the authors' knowledge the first to use this definition was Lewin [30] in 1962 for combining $N = 2$ channels.)

The optimum phases are given by

$$\phi_2, \ldots, \phi_N = \underset{\phi_2,\ldots,\phi_N}{\operatorname{argmax}} \left\{ \left| \int_{-\infty}^{\infty} \left| c_1(t) + \sum_{n=2}^{N} e^{j\phi_n} c_n(t) \right|^2 \right| \right\}. \tag{22}$$

There does not appear to be a closed-form solution to this optimization problem except for the case $N = 2$, where the solution is

$$\phi_2 = \angle \left\{ \int_{-\infty}^{\infty} c_1(t) c_2^*(t) dt \right\}. \tag{23}$$

The Ungerboeck observation model follows from (1) using the definitions of $c_{EGC}(t)$ and $z_{EGC}(t)$ given in (21) for $c(t)$ and $z(t)$, respectively. Using $h_{EGC}(t) = g(t) \star c_{EGC}(t)$ and $x_{EGC}(t) = h_{EGC}(t) \star h_{EGC}^*(-t)$, the model is given by (7) where

$$E\{v((k+m)T_s)v^*(kT_s)\} = N \times 2N_0 x_{EGC}(mT_s). \tag{24}$$

The Forney observation model is given by (12) where

$$E\{\eta((k+m)T_s)\eta^*(kT_s)\} = N \times 2N_0\delta_m. \tag{25}$$

These results are summarized in the third row of Table 2.

C. MAXIMUM RATIO COMBINING

In maximum ratio combining (MRC), the received signals are scaled by a non-negative real-valued constant and co-phased to produce the combiner output. Again, using $r_1(t)$ as the reference signal for the co-phasing, the maximum ratio combiner output may be expressed as

$$r(t) = k_1 r_1(t) + \sum_{n=2}^{N} e^{j\phi_n} k_n r_n(t) \tag{26}$$

$$= \sum_{\ell} I_{\ell} g(t - \ell T_s) \star \underbrace{\left[k_1 c_1(t) + \sum_{n=2}^{N} e^{j\phi_n} k_n c_n(t) \right]}_{c_{MRC}(t)}$$

$$+ \underbrace{k_1 z_1(t) + \sum_{n=2}^{N} e^{j\phi_n} k_n z_n(t)}_{z_{MRC}(t)}. \tag{27}$$

The weighting constants $k_1, \ldots, k_n$ are proportional to the signal-to-noise ratios on their respective channels. The phases that maximize the received signal energy are defined by an optimization identical to (22), except that the weighting constants are included in the object function.

The Ungerboeck observation model follows from (1) using the definitions of $c_{MRC}(t)$ and $z_{MRC}(t)$ given in (27) for $c(t)$ and $z(t)$, respectively. Using $h_{MRC}(t) = g(t) \star c_{MRC}(t)$ and $x_{MRC}(t) = h_{MRC}(t) \star h_{MRC}^*(-t)$, the model is given by (7) where

$$E\{v((k+m)T_s)v^*(kT_s)\} = \left[\sum_{n=1}^{N} k_n^2 \right] \times 2N_0 x_{MRC}(mT_s). \tag{28}$$

The Forney observation model is given by (12) where

$$E\{\eta((k+m)T_s)\eta^*(kT_s)\} = \left[\sum_{n=1}^{N} k_n^2 \right] \times 2N_0\delta_m. \tag{29}$$

These results are summarized in the fourth row of Table 2.

D. LEFT- AND RIGHT-HAND ELLIPTICAL COMBINING

In the case where two co-located cross-polarized antenna elements present, the two antenna outputs are often combined using a directional coupler (or "hybrid") that isolates the combined output from the inputs. The coupling induces a 90° phase shift on one of the two inputs giving rise to what is popularly called a left- or right-hand circular polarized signal. To be technically precise, "circular" refers to the case where the two inputs have the same magnitude. When the magnitudes are different, the resulting signal is a left- or right-hand elliptically polarized signal.

Using the complex-valued baseband notation, the coupler output is

$$r(t) = r_1(t) \pm jr_2(t) \tag{30}$$

$$= \sum_{\ell} I_{\ell} g(t - \ell T_s) \star \underbrace{\left[c_1(t) \pm jc_2(t) \right]}_{c_{EPC}(t)}$$

$$+ \underbrace{z_1(t) \pm jz_2(t)}_{z_{EPC}(t)} \tag{31}$$

where "$+$" produces a left-hand elliptically polarized signal and "$-$" produces a right-hand elliptically polarized signal.

The Ungerboeck observation model follows from (1) using the definitions for $c_{EPC}(t)$ and $z_{EPC}(t)$ given in (31) for $c(t)$ and $z(t)$, respectively. Using $h_{EPC}(t) = g(t) \star c_{EPC}(t)$ and $x_{EPC}(t) = h_{EPC}(t) \star h_{EPC}^*(-t)$, the model is given by (7) where

$$E\{v((k+m)T_s)v^*(kT_s)\} = 4N_0 x_{EPC}(mT_s). \tag{32}$$

The Forney observation model is given by (12) where

$$E\{\eta((k+m)T_s)\eta^*(kT_s)\} = 4N_0\delta_m. \tag{33}$$

These results are summarized in the fifth row of Table 2.

E. MAXIMUM LIKELIHOOD COMBINING

The maximum likelihood (ML) detector for diversity reception in a frequency-selective fading environment was derived by Scott *et al.* [9]. Even though the ML detector described in [9] was developed for GMSK, it is easily generalized. In this section, the results are applied more generally to produce the corresponding Ungerboeck and Forney observation models. A block diagram illustrating ML combining is shown in Figure 3 (a). A filter, matched to the received pulse shape on each antenna, is applied to each antenna output. The matched filter outputs are combined to produce

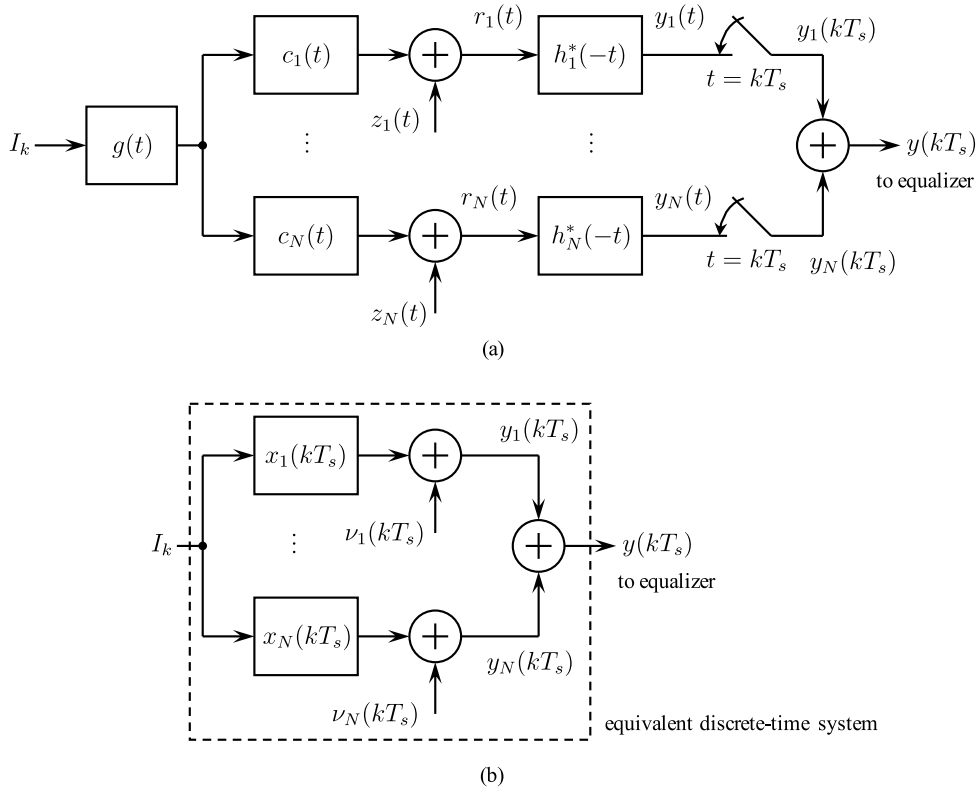$$y(t) = \sum_{n=1}^{N} y_n(t) \tag{34}$$

FIGURE 3. ML combining for N spatially-separated channels: (a) The sequence of operations defined by ML principle; (b) The equivalent discrete-time system.

where the output of the n-th matched filter is

$$y_n(t) = \sum_\ell I_\ell x_n(t - \ell T_s) + v_n(t) \qquad (35)$$

where $x_n(t) = h_n(t) \star h_n^*(-t)$ with $h_n(t) = g(t) \star c_n(t)$ and where $v_n(t) = z_n(t) \star h_n^*(-t)$ is a complex-valued circularly-symmetric normal random process with

$$E\{v_n(t + \tau)v_n^*(t)\} = 2N_0 x_n(\tau). \qquad (36)$$

The sampled output of the n-th matched filter is

$$y_n(kT_s) = \sum_\ell I_\ell x_n((k - \ell)T_s) + v_n(kT_s) \qquad (37)$$

where $v_n(kT_s)$ is a sequence of complex-valued circularly-symmetric normal random variables with autocorrelation function $2N_0 x_n(kT_s)$. The equivalent discrete-time system is shown in Figure 3 (b).

The Ungerboeck observation model can be used to represent the equivalent discrete-time system in Figure 3 (b) by making the following associations:

$$x_{\mathrm{ML}}(kT_s) = \sum_{n=1}^N x_n(kT_s) \qquad (38)$$

$$v_{\mathrm{ML}}(kT_s) = \sum_{n=1}^N v_n(kT_s). \qquad (39)$$

Because the underlying random processes $z_n(t)$ are uncorrelated, each sequence of random variables in the summation in (39) are uncorrelated and, because they are normal, independent. Consequently,

$$E\{v_{\mathrm{ML}}((k + m)T_s)v_{\mathrm{ML}}^*(kT_s)\} = 2N_0 x_{\mathrm{ML}}(mT_s). \qquad (40)$$

The Ungerboeck observation model is given by (7) using $x_{\mathrm{ML}}(kT_s)$ and $v_{\mathrm{ML}}(kT_s)$ for $x(kT_s)$ and $v(kT_s)$, respectively, where the noise correlation is given by (40). The Forney observation model is obtained by factoring $X_{\mathrm{ML}}(z)$ and is given by (12) where

$$E\{\eta((k + m)T_s)\eta^*(kT_s)\} = 2N_0\delta_m. \qquad (41)$$

It is important to point out that the noise whitening is applied to the combined signal, not to each of the branches in Figure 3(b), as in [31].

IV. NUMERICAL EXAMPLES

In this section, the Forney observation models are used to assess the post equalizer bit error rate for the combining schemes outlined in the previous section. Because we include polarization diversity in the broad category of spatial diversity, the multipath channel that includes polarization state information is used. Given the absence of good mm-wave channel models that include polarization state information,
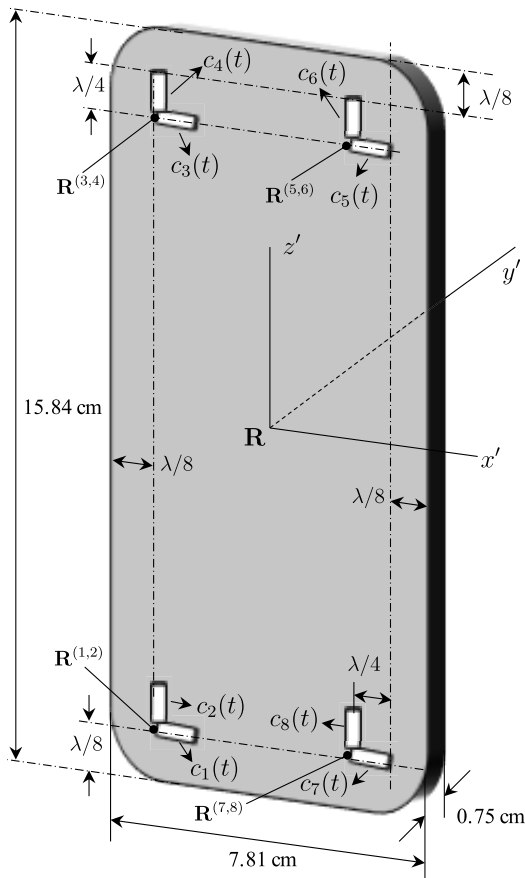
FIGURE 4. An illustration of a mobile handset showing the four sets of co-located cross-polarized antenna elements used in the simulations. The channels seen by each antenna element are indicated in the figure.

we develop a relatively sparse four-ray line-of-sight channel from which the Forney observation model is derived.

A. A GEOMETRIC MULTIPATH CHANNEL WITH POLARIZATION STATE INFORMATION

The channel used in this example is the 4-path channel illustrated in Figure 11 in the Appendix. A massive MIMO system is assumed at basestation transmitter. This transmitter produces a vertically polarized beam with a beamwidth of $30°$ that tracks the location of the mobile receiver. The mobile receiver handset is illustrated in Figure 4. The mobile is equipped with four sets of co-located cross-polarized antenna elements (for a total of $N = 8$ antenna elements) positioned in the four corners as shown. The mathematical derivation is summarized in the Appendix. The continuous-time impulse responses with polarization state information are of the form

$$c^{(i,i+1)}(t) = c_x^{(i,i+1)}(t)\hat{\mathbf{x}} + c_y^{(i,i+1)}(t)\hat{\mathbf{y}} + c_z^{(i,i+1)}(t)\hat{\mathbf{z}} \quad (42)$$

where the superscript $(i, i+1)$ represents the value at antenna pair $i, i+1$ for $i = 1, 3, 5, 7$ and where $\hat{\mathbf{x}}$, $\hat{\mathbf{y}}$, and $\hat{\mathbf{z}}$ are the unit vectors for the 3-dimensional coordinate system shown in Figure 4. The x-, y-, and z-components of the impulse

response are of the form

$$c_x^{(i,i+1)}(t) = \sum_{m=0}^{3} c_{x,m}^{(i,i+1)}\delta(t - \tau_m^{(i,i+1)})$$

$$c_y^{(i,i+1)}(t) = \sum_{m=0}^{3} c_{y,m}^{(i,i+1)}\delta(t - \tau_m^{(i,i+1)})$$

$$c_z^{(i,i+1)}(t) = \sum_{m=0}^{3} c_{z,m}^{(i,i+1)}\delta(t - \tau_m^{(i,i+1)}). \quad (43)$$

The coefficient values and delays for $i = 1, 3, 5, 7$ are listed in Equations (44)–(47), respectively.

$$c_{x,0}^{(1,2)} = 1.2445 \times 10^{-1}$$
$$c_{x,1}^{(1,2)} = 1.2230 \times 10^{-1} - j6.9648 \times 10^{-5}$$
$$c_{x,2}^{(1,2)} = 6.6750 \times 10^{-2} + j1.0186 \times 10^{-3}$$
$$c_{x,3}^{(1,2)} = 1.0848 \times 10^{-1} - j4.7812 \times 10^{-4}$$
$$c_{y,0}^{(1,2)} = 1.3527 \times 10^{-6}$$
$$c_{y,1}^{(1,2)} = -1.9832 \times 10^{-3} - j3.4388 \times 10^{-6}$$
$$c_{y,2}^{(1,2)} = -7.2554 \times 10^{-7} - j1.1071 \times 10^{-8}$$
$$c_{y,3}^{(1,2)} = 8.2038 \times 10^{-3} + j1.1839 \times 10^{-4}$$
$$c_{z,0}^{(1,2)} = 9.9223 \times 10^{-1}$$
$$c_{z,1}^{(1,2)} = -9.7536 \times 10^{-1} + j5.5481 \times 10^{-4}$$
$$c_{z,2}^{(1,2)} = -4.9284 \times 10^{-1} - j7.5205 \times 10^{-3}$$
$$c_{z,3}^{(1,2)} = -8.7343 \times 10^{-1} + j3.6888 \times 10^{-3}$$
$$\tau_0^{(1,2)} = 772.68 \text{ ns}$$
$$\tau_1^{(1,2)} = 772.79 \text{ ns}$$
$$\tau_2^{(1,2)} = 773.67 \text{ ns}$$
$$\tau_3^{(1,2)} = 779.12 \text{ ns} \quad (44)$$
$$c_{x,0}^{(3,4)} = 1.2379 \times 10^{-1}$$
$$c_{x,1}^{(3,4)} = 1.2165 \times 10^{-1} - j6.9284 \times 10^{-5}$$
$$c_{x,2}^{(3,4)} = 6.6830 \times 10^{-2} + j1.0261 \times 10^{-3}$$
$$c_{x,3}^{(3,4)} = 1.0791 \times 10^{-1} - j4.7562 \times 10^{-4}$$
$$c_{y,0}^{(3,4)} = 1.3456 \times 10^{-6}$$
$$c_{y,1}^{(3,4)} = -1.9727 \times 10^{-3} - j3.4208 \times 10^{-6}$$
$$c_{y,2}^{(3,4)} = -7.2641 \times 10^{-7} - j1.1153 \times 10^{-8}$$
$$c_{y,3}^{(3,4)} = 8.1597 \times 10^{-3} + j1.1777 \times 10^{-4}$$
$$c_{z,0}^{(3,4)} = 9.9231 \times 10^{-1}$$
$$c_{z,1}^{(3,4)} = -9.7544 \times 10^{-1} + j5.5490 \times 10^{-4}$$
$$c_{z,2}^{(3,4)} = -4.9098 \times 10^{-1} - j7.5386 \times 10^{-3}$$
$$c_{z,3}^{(3,4)} = -8.7350 \times 10^{-1} + j3.6894 \times 10^{-3}$$
$$\tau_0^{(3,4)} = 772.61 \text{ ns}$$
$$\tau_1^{(3,4)} = 772.73 \text{ ns}$$

$$\tau_2^{(3,4)} = 773.74 \text{ ns}$$

$$\tau_3^{(3,4)} = 779.06 \text{ ns} \qquad (45)$$

$$c_{x,0}^{(5,6)} = 1.2375 \times 10^{-1}$$

$$c_{x,1}^{(5,6)} = 1.2161 \times 10^{-1} - j6.9239 \times 10^{-5}$$

$$c_{x,2}^{(5,6)} = 6.6825 \times 10^{-2} + j1.0256 \times 10^{-3}$$

$$c_{x,3}^{(5,6)} = 1.0788 \times 10^{-1} - j4.7533 \times 10^{-4}$$

$$c_{y,0}^{(5,6)} = 1.3447 \times 10^{-6}$$

$$c_{y,1}^{(5,6)} = -1.9714 \times 10^{-3} - j3.4176 \times 10^{-6}$$

$$c_{y,2}^{(5,6)} = -7.2612 \times 10^{-7} - j1.1144 \times 10^{-8}$$

$$c_{y,3}^{(5,6)} = 8.1563 \times 10^{-3} + j1.1768 \times 10^{-4}$$

$$c_{z,0}^{(5,6)} = 9.9231 \times 10^{-1}$$

$$c_{z,1}^{(5,6)} = -9.7545 \times 10^{-1} + j5.5473 \times 10^{-4}$$

$$c_{z,2}^{(5,6)} = -4.9110 \times 10^{-1} - j7.5374 \times 10^{-3}$$

$$c_{z,3}^{(5,6)} = -8.7354 \times 10^{-1} + j3.6884 \times 10^{-3}$$

$$\tau_0^{(5,6)} = 772.86 \text{ ns}$$

$$\tau_1^{(5,6)} = 772.98 \text{ ns}$$

$$\tau_2^{(5,6)} = 773.99 \text{ ns}$$

$$\tau_3^{(5,6)} = 779.31 \text{ ns} \qquad (46)$$

$$c_{x,0}^{(7,8)} = 1.2441 \times 10^{-1}$$

$$c_{x,1}^{(7,8)} = 1.2226 \times 10^{-1} - j6.9604 \times 10^{-5}$$

$$c_{x,2}^{(7,8)} = 6.6745 \times 10^{-2} + j1.0181 \times 10^{-3}$$

$$c_{x,3}^{(7,8)} = 1.0845 \times 10^{-1} - j4.7783 \times 10^{-4}$$

$$c_{y,0}^{(7,8)} = 1.3519 \times 10^{-6}$$

$$c_{y,1}^{(7,8)} = -1.9820 \times 10^{-3} - j3.4356 \times 10^{-6}$$

$$c_{y,2}^{(7,8)} = -7.2525 \times 10^{-7} - j1.1062 \times 10^{-8}$$

$$c_{y,3}^{(7,8)} = 8.2004 \times 10^{-3} + j1.1830 \times 10^{-4}$$

$$c_{z,0}^{(7,8)} = 9.9223 \times 10^{-1}$$

$$c_{z,1}^{(7,8)} = -9.7537 \times 10^{-1} + j5.5463 \times 10^{-4}$$

$$c_{z,2}^{(7,8)} = -4.9296 \times 10^{-1} - j7.5193 \times 10^{-3}$$

$$c_{z,3}^{(7,8)} = -8.7347 \times 10^{-1} + j3.6878 \times 10^{-3}$$

$$\tau_0^{(7,8)} = 772.93 \text{ ns}$$

$$\tau_1^{(7,8)} = 773.04 \text{ ns}$$

$$\tau_2^{(7,8)} = 773.92 \text{ ns}$$

$$\tau_3^{(7,8)} = 779.37 \text{ ns} \qquad (47)$$

The frequency-domain transfer functions $C^{(1,2)}(f)$, $C^{(3,4)}(f)$, $C^{(5,6)}(f)$, and $C^{(7,8)}(f)$ are plotted in Figures 5 (a) – (d), respectively. Observations:

1) The z-component is the most powerful component in all four cases. This is due to the geometry: the vertically polarized transmitted signal produces the most energy in the spatial dimension aligned with the polarization.

2) The y-component is the least powerful component. The only major contributors to the y-component are the propagation paths **TWR** and **TBR**. Given the angles and reflection coefficients, the least amount of transmitted power is present in the y−component.

3) The channels at points $\mathbf{R}^{(1,2)}$ and $\mathbf{R}^{(7,8)}$ have similar magnitudes (but differents phases) because they are separated by 7.27 cm. (See Figure 4.) The same observation applies to the channels at points $\mathbf{R}^{(3,4)}$ and $\mathbf{R}^{(5,6)}$. The channels at points $\mathbf{R}^{(1,2)}$ and $\mathbf{R}^{(3,4)}$ are different because they are separated by 15.3 cm. The same observation applies to the channels at points $\mathbf{R}^{(5,6)}$ and $\mathbf{R}^{(7,8)}$. It is these differences that can be exploited for spatial diversity.

B. DIVERSITY MEASURES

Diversity gain is defined as the negative of the asymptotic slope of the BER versus SNR [32]–[34]

$$\lim_{\text{SNR} \to \infty} -\frac{\log P_e(\text{SNR})}{\log(\text{SNR})}, \qquad (48)$$

where $P_e(\text{SNR})$ is the average error probability at the equalizer output as a function of SNR. The analyses in [32], [33], [35] apply to the equivalent discrete-time models at the equalizer input whereas the analysis in [34] is for OFDM systems. None of these quantify the potential improvements from combining the outputs of parallel channels before equalization in terms of the continuous-time channel impulse responses. Consequently, we adopt indirect measures in an attempt to gain insights into the potential improvement from combining. The emphasis is on polarization diversity for each antenna pair because this has received the least attention in the open literature.

Two common measures of polarization diversity are the cross polar discrimination XPD [7], [36]–[44] and the cross correlation coefficient ρ [7], [37]–[39]. Other measures include the co-polar power ratio [36], the number of channel correlation matrix eigenvalues exceeding the noise power level [44], and the square of the normalized trace of the channel covariance matrix [45].

Because the XPD and the cross correlation coefficient are pairwise measures, these measures are applied to the two channels with impulse responses $c_1(t)$ and $c_2(t)$ in Figure 4 to illustrate how to interpret the results. Note that when the (x', y', z') coordinate system in Figure 4 is aligned with the (x, y, z) coordinate system in Figure 11, $c_1(t) = c_x(t)$ and $c_2(t) = c_z(t)$. As the mobile is rotated [about the origin of the (x', y', z') coordinate system] the relationships between $c_1(t)$ and $c_2(t)$ and $c_x(t)$, $c_y(t)$, and $c_z(t)$ change, respectively.

The XPD is the ratio of the energy received by the co-polarized antenna to the energy received by the cross-polarized antenna. Historically, this measure was developed for frequency non-selective fading channels [7], [37]–[40], [42], [43] although some of the more recent publications have

extended the XPD concept to frequency-selective channels [36], [41], [44]. To apply XPD to our channel, we return to the basic definition of a ratio of received signal powers. Because the transmitted signal is common to the signals received on the orthogonally-polarized antenna elements, XPD reduces to the ratio of channel energies:

$$\text{XPD} = \frac{\int_{f_1}^{f_2} |C_2(f)|^2 df}{\int_{f_1}^{f_2} |C_1(f)|^2 df} \tag{49}$$

where f_1 and f_2 define the lower and upper band edges of the occupied spectrum and where $C_1(f)$ and $C_2(f)$ are the Fourier transforms of $c_1(t)$ and $c_2(t)$, respectively, in Figure 4. We designate $C_2(f)$ as the co-polarized channel because its corresponding antenna element is aligned with the vertically polarized transmit antennas when the (x', y', z') coordinate system is aligned with the (x, y, z) coordinate system. However, as the mobile handset rotates about the origin of the (x', y', z') coordinate system, their roles change. For example, as the handset rotates about the y' axis, $C_1(f)$ becomes the co-polarized channel and $C_2(f)$ becomes the cross-polarized channel for rotation angles of $\pm 90°$. For most rotations, neither of the antenna elements is truly co-polarized or cross-polarized with the transmit antennas. Consequently, the definition of XPD in (49) fixes $C_2(f)$ in the numerator and allows for the fact that this ratio will be $\ll 1$ for some rotation angles.

Two versions of the cross correlation coefficient have been used in the literature: the cross correlation coefficient of the signal envelope [7], [37] and the coherent cross correlation coefficient [38], [39]. For our purposes the cross correlation of the signal envelope is

$$\rho_{\text{env}} = \frac{\int_{f_1}^{f_2} |C_1(f)||C_2(f)|df}{\sqrt{\mathcal{E}_1 \mathcal{E}_2}} \tag{50}$$

while the coherent cross correlation coefficient is

$$\rho_{\text{coh}} = \frac{\text{Re}\left\{\int_{f_1}^{f_2} C_1(f)C_2^*(f)df\right\}}{\sqrt{\mathcal{E}_1 \mathcal{E}_2}} \tag{51}$$

where $\mathcal{E}_1$ and $\mathcal{E}_2$ are the channel energies given by (18) or, using Parseval's theorem,

$$\mathcal{E}_i = \int_{f_1}^{f_2} |C_i(f)|^2 df \tag{52}$$

for $i = 1, 2$.

The analysis in [37] suggested that both the XPD and a correlation coefficient must be examined simultaneously to gain insight into potential gains for polarization diversity. When XPD is close to unity (0 dB) and the correlation coefficient is small, the two channels have nearly the same energy (XPD = 0 dB) and are different (ρ_{coh} or ρ_{env} is close to zero).

The potential for performance improvement is very good. When these conditions are not simultaneously met, the potential for performance improvement is not as good. For example, when XPD is not close 0 dB, one of the channels is much stronger than the other and there is not much to be gained by combining them. When the correlation coefficient is close to unity, the signals are similar and diversity combining shifts the BER vs. SNR curve to the left by at most 3 dB. In the scenario illustrated in Figures 11 and 4 where the (x', y', z') axes are aligned with the (x, y, z) axes, XPD = 24.3577 dB and $\rho_{\text{coh}} = 0.2514$. These values are typical values and suggests that the potential for diversity gains is good [37].

The diversity parameters XPD, ρ_{coh}, and ρ_{env} vary as the orientation of the mobile varies. This is because the spatial relationships between the co-located cross-polarized elements in Figure 4 and the three spatial components of the electric field change with rotation angle. These changes are illustrated by evaluating XPD, ρ_{coh}, and ρ_{env} for rotations about the x'- y'- and z'- axes, as shown in Figures 6 (a) – (c), respectively. In these figures, note that ρ_{env} is nearly constant with respect to the rotation angles. This demonstrates that the envelope correlation used in [7], [37] for frequency non-selective channels does not extend to the frequency-selective channel case. The remainder of the analysis examines ρ_{coh}.

In Figure 6 (a), for most rotation angles about the x'-axis, 5 dB $\leq$ XPD $\leq$ 17 dB and $-0.2 \leq \rho_{\text{coh}} \leq 0.2$. These are good values from the polarization diversity point of view (neither XPD nor $|\rho_{\text{coh}}|$ are too large). This is because $C_1(f)$ is $C_x^{(1,2)}(f)$ in Figure 5 (a) for all rotation angles while $C_2(f)$ is a linear combination of $C_z^{(1,2)}(f)$ and $C_y^{(1,2)}(f)$ in Figure 5 (a). When the rotation angle is exactly $\pm 90°$, $C_2(f) = C_y^{(1,2)}(f)$, a very weak channel as shown in Figure 5 (a).

In Figure 6 (b), -17 dB $\leq$ XPD ≤ 17 dB and $-0.96 \leq \rho_{\text{coh}} \leq 0.96$ for all rotation angles. This is because for all rotations about the y'-axis, $C_1(f)$ and $C_2(f)$ are linear combinations of $C_x^{(1,2)}(f)$ and $C_z^{(1,2)}(f)$, two of the strong channels in Figure 5 (a). The rotations that produce large values for $|\rho_{\text{coh}}|$ produce less potential for polarization diversity. Consequently, rotations about the y'-axis do not seem to have potential for strong polarization diversity gains.

In Figure 6 (c), the situation is somewhat less clear. The parameter ρ_{coh} has acceptably low values except for rotation angles of $\pm 90°$. But, XPD $>$ 20 dB for rotation angles in the intervals $[50°, 130°]$ and $[230°, 310°]$. This is because $C_2(f) = C_z^{(1,2)}(f)$ for all rotation angles but $C_1(f)$ is a linear combination of $C_x^{(1,2)}(f)$ and $C_y^{(1,2)}(f)$. When the rotation angle is $\pm 90°$, $C_1(f) = C_y^{(1,2)}(f)$, one of the weakest channels in Figure 5 (a). Consequently, the potential gains for polarization diversity are rotation dependent.

In summary, for the example channel examined here, polarization diversity should produce reasonably good performance gains for most rotation angles. For rotation angles where polarization gain does not hold promise, it is
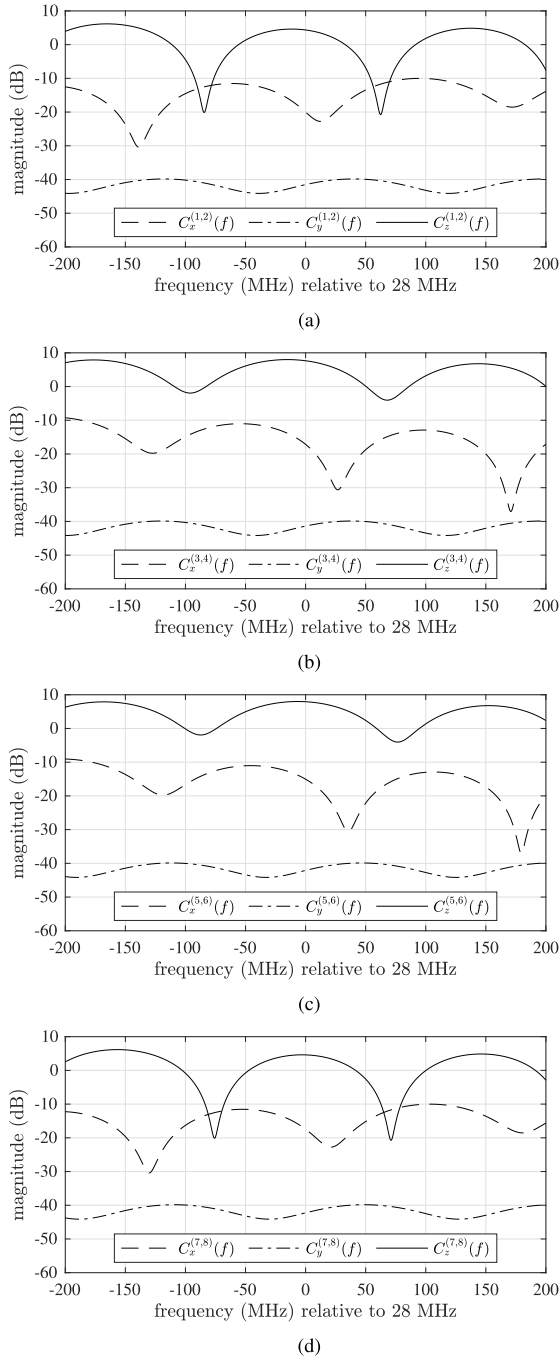
FIGURE 5. Frequency-domain transfer functions for the four-path propagation model from point **T** to one of the four points on the mobile handset in Figure 4: (a) the *x*-, *y*-, and *z*-components at point $R^{(1,2)}$; (b) the *x*-, *y*-, and *z*-components at point $R^{(3,4)}$; (c) the *x*-, *y*-, and *z*-components at point $R^{(5,6)}$; (d) the *x*-, *y*-, and *z*-components at point $R^{(7,8)}$.

because one of the co-located orthogonally polarized antenna elements "sees" a strong channel while the other element "sees" a weak channel. In such situations, there is little to be gained by incorporating the output of the weak channel in the detector. The results for the antenna pairs $C_3(f)$, $C_4(f)$; $C_5(f)$, $C_6(f)$; and $C_7(f)$, $C_8(f)$ are nearly identical and are not included here.
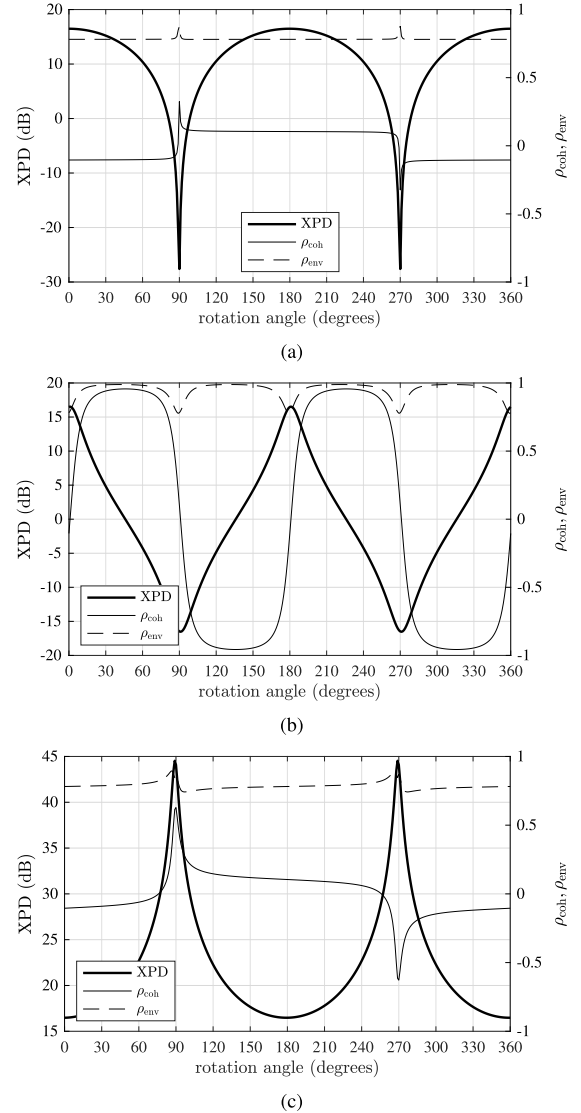

FIGURE 6. XPD (left axis) and correlation coefficients (right axis) as a function of rotation angle: (a) rotation about the *x'*-axis; (b) rotation about the *y'*-axis; (c) rotation about the *z'*-axis. The (x', y', z') coordinate system is defined in Figure 4.

C. BIT ERROR RATE (BER) COMPARISON–TWO CO-LOCATED CROSS-POLARIZED ANTENNAS

Here the improvement in post-equalizer BER for the antenna pair $C_1(f)$, $C_2(f)$ is examined. The Forney observation model corresponding to this pair of antenna outputs for each of the spatial combining techniques described in Section III is used as the input to an MMSE equalizer (i.e., $N = 2$). The Forney observation model channels for the combining techniques are plotted in Figure 7. In each plot the intersymbol interference (ISI) ratio defined by

$$\text{ISI} = \frac{\sum_{n=1}^{L} \left| f_{(\cdot)}(nT_s) \right|^2}{\left| f_{(\cdot)}(0) \right|^2} \qquad (53)$$

is shown. The ISI ratio is a coarse measure of ISI that an equalizer must remove. The ISI ratio is the lowest (best) for
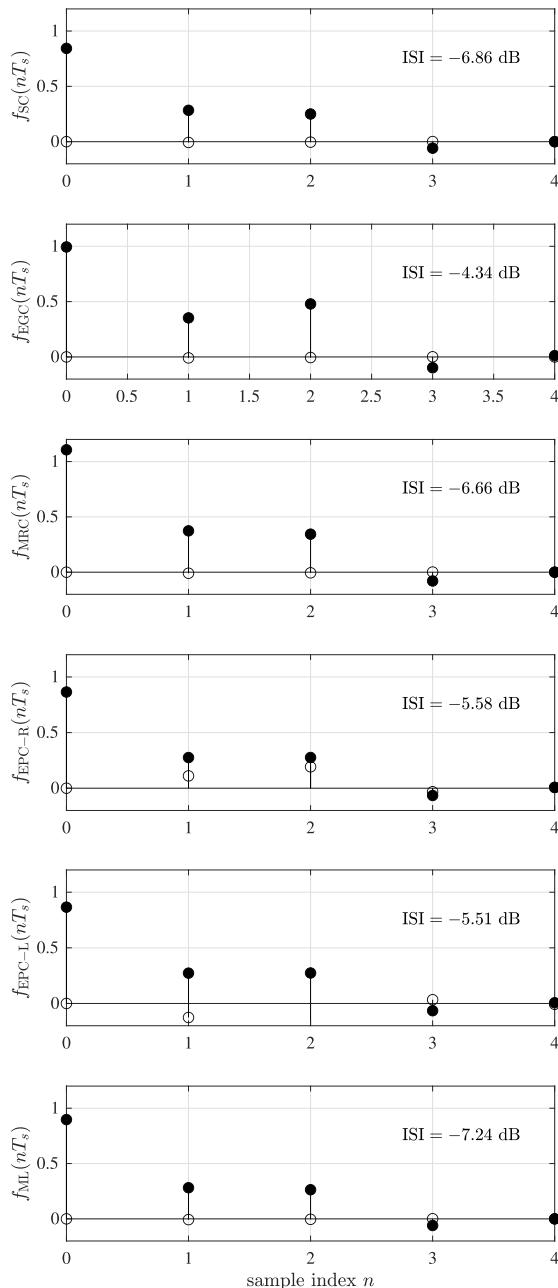
FIGURE 7. The coefficients for the Forney observation model for each of the combining techniques applied to $C_1(f)$ and $C_2(f)$. The solid markers are the real parts of the coefficients and the clear markers are the imaginary parts.

ML combining and the worst for EGC. ML combining and SC produce the lowest ISI ratios. The ISI ratio is only one of two parameters that define equalizer performance. The other is the channel strength. For example, the two EPC channels have lower ISI ratios than the EGC channel, but the EGC channel is stronger and presents a higher signal-to-noise ratio to the equalizer.

Because prediction of the post-equalizer BER performance is difficult, we resort to computer simulations. The simulation parameters are summarized in Table 3. A length-31 MMSE

equalizer was computed for each of the six whitened channel outputs and for each signal-to-noise ratio.

TABLE 3. The parameters used for the post-equalizer BER simulations.

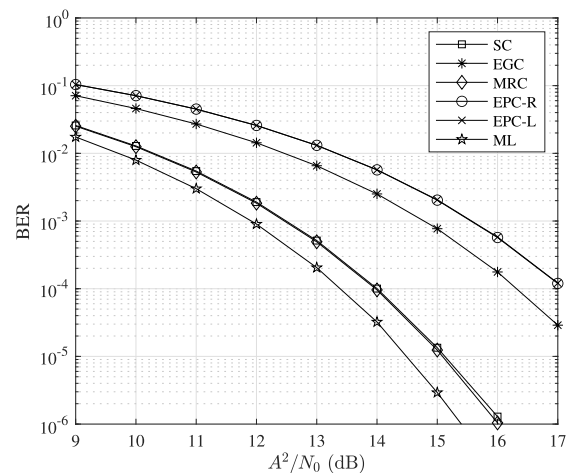| Parameter	Value
Constellation	QPSK $I_k \in \{\pm A \pm jA\}$
Pulse shape	SRRC with 50% roll-off
	span = 12 symbols
Bit rate	533 1/3 Mbits/s
Frequency support	-200 MHz $\leq f \leq 200$ MHz
Equalizer	length-63 symbol-spaced MMSE equalizer

FIGURE 8. Simulated post-equalizer BER results for $C_1(f)$ and $C_2(f)$ using the combining techniques described in Section III.

The simulated post-equalizer BER performance is plotted in Figure 8. The BER results are plotted as a function of the ratio A^2/N_0. The different channel energies scaled the effective "signal-to-noise ratio" and are part of the comparison. Observations:

1) ML combining substantially outperforms the other combining techniques.
2) The worst-performing combining technique is elliptical combining. This is an interesting result because elliptical combining is often employed with co-located cross-polarized antenna elements.
3) The performance of selection combining essentially matches that of maximum ratio combining. This is explained by the fact that $C_1(f) = C_x^{(1,2)}(f)$ and $C_2(f) = C_z^{(1,2)}(f)$ in Figure 5 (a). Consequently $C_2(f)$ is a stronger channel than $C_1(f)$: $\mathcal{E}_2$ is 16.5 dB greater than $\mathcal{E}_1$. For this channel pair, the MRC gain only compensates for the additional noise accompanying the weaker channel. The relatively poor performance of equal gain combining is explained in the same way.

The only spatial diversity available is from the polarization state. As expected, ML combining best exploits the available gain from polarization diversity. MRC and SC (somewhat surprisingly) are the next best options for polarization diversity and achieve a post-equalizer BER about 0.6 dB worse than that of ML combining.
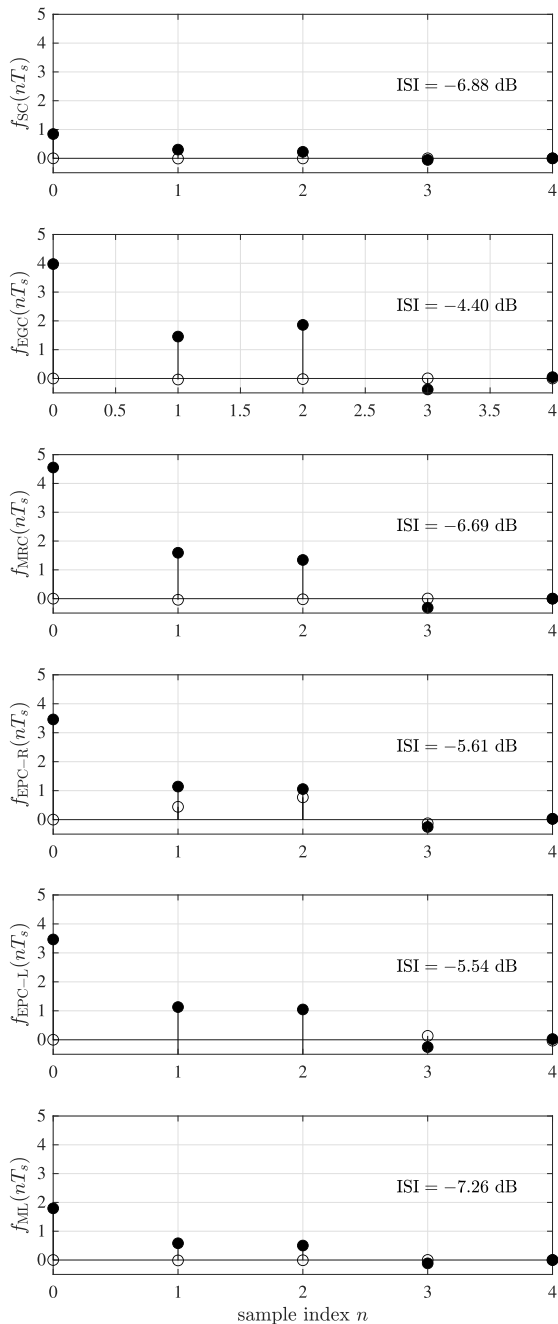
FIGURE 9. The coefficients for the Forney observation model for each of the combining techniques applied to $C_1(f) - C_8(f)$. The solid markers are the real parts of the coefficients and the clear markers are the imaginary parts.

FIGURE 10. Simulated post-equalizer BER results for $C_1(f) - C_8(f)$ using the combining techniques described in Section III.

The parameters used for the simulation are summarized in Table 3. The equivalent Forney observation models for each combining technique are plotted in Figure 9. Included in these plots is the ISI ratio (53) which is a coarse measure of the ISI the equalizer must mitigate. Note that ML combining produces the lowest ISI ratio followed by MRC and SC. It will be shown that SC is not competitive in this case due to the signal-to-noise ratio penalty resulting from SC being a weak channel.

A length-31 MMSE equalizer was computed for each of the six whitened channel outputs and for each signal-to-noise ratios. The simulated post-equalizer BER performance is plotted in Figure 10. As before, the BER results are plotted as a function of the ratio A^2/N_0 to preserve the advantage of strong channels over weak channels. Observations:

1) ML combining outperforms the other combining techniques.
2) MRC combining is the next best option and is about 0.5 dB inferior to ML combining. Unlike the case in Figure 8, SC does not achieve the same performance as MRC combining. Here SC is the worst-performing option. The difference is that the eight antennas provide a set of channels comprising four strong channels and four weak channels. MRC exploits the diversity inherent in the four strong channels in a way that outperforms the selection of the one strongest channel.
3) EGC is about 3 dB worse than ML combining and 2.2 dB worse than MRC.
4) EPC-R/L + EGC is more competitive here than EPC-R/L was in the two antenna case. The performance advantage is attributed to the application of EGC. An interesting conclusion is that it is better to apply EGC to all eight antenna outputs than it is to apply EPC-R/L to each co-located cross-polarized antenna pair and combine elliptically-combined outputs using EGC.

A large number of combining options are possible. For example selection combining may be applied to each co-located

D. BIT ERROR RATE (BER) COMPARISON– EIGHT ANTENNAS

In this experiment, all outputs of all eight antenna elements in Figure 4 are combined before equalization. The SC, EGC, MRC, and ML combining techniques are applied as described in Section III. Elliptical combining is performed in combination with equal gain combining: elliptical combining is applied to each antenna pair to create four channels; the four channels are combined using EGC.
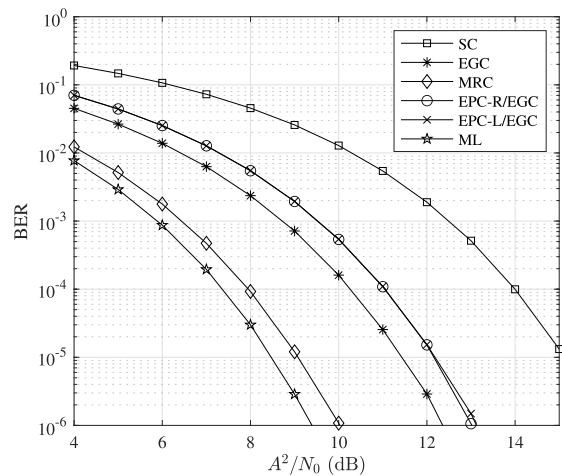
antenna pair to produce four outputs and the four outputs may be combined using MRC. The number of possibilities is a combinatorial exercise. But the technique outlined in Section III may be extended to any of these in a straightforward way.

V. CONCLUSION

The performance of spatial diversity over a frequency-selective multipath fading channel has been investigated where an emphasis has been placed on 5G cellular systems operating in the mmWave band in a small cell urban environment. The propagation scenario used as an example is a downlink to a mobile equipped with four pairs of co-located cross-polarized antennas. To facilitate the performance analysis, the Forney observation model for a number of popular combining techniques was derived and used to assess the post-equalizer BER performance of a simple MMSE equalizer.

Two sets of BER simulations were performed. In the first set, the performance of combining and equalization for one pair of co-located cross-polarized antennas was analyzed. The emphasis was on polarization diversity. The simulation results showed that ML combining maximizes polarization diversity and achieved a post-equalizer BER about 0.5 dB better than and that of MRC. Interestingly, the performance of SC was very similar to that of MRC. This is because polarization diversity often produces a strong channel and a weak channel. The surprising result was how poorly elliptical combining performed given its current popularity.

The second set of BER simulations incorporated all eight antennas into the diversity combining techniques. Here, polarization diversity was only a part of the available diversity. Again, ML combining maximized the diversity gain and achieved a post-equalizer BER performance about 0.8 dB better than MRC. The performance EGC next and was about 2.2 dB worse than MRC. The ordering ML > MRC > EGC > SC follows the traditional ordering because incorporating all eight channels into the diversity combiner avoided the situation of one strong channel and one weak channel. The results also show that for each pair of co-located cross-polarized antenna elements, it is better to apply EGC or MRC to each pair than elliptical combining.

APPENDIX
DERIVATION OF THE MULTIPATH PROPAGATION MODEL WITH POLARIZATION STATE INFORMATION

In this appendix, all vectors are column vectors and denoted with bold-face variables. The ''hat notation'' is used to identify unit vectors. For example, $\hat{\mathbf{x}}$ is the unit vector in the x-direction in our coordinate system. Bold quantities, such as $\mathbf{V}$ are understood to be 3×1 vectors with two equivalent forms:

$$\mathbf{V} = \begin{bmatrix} V_x \\ V_y \\ V_z \end{bmatrix} = V_x\hat{\mathbf{x}} + V_y\hat{\mathbf{y}} + V_z\hat{\mathbf{z}}. \qquad (54)$$
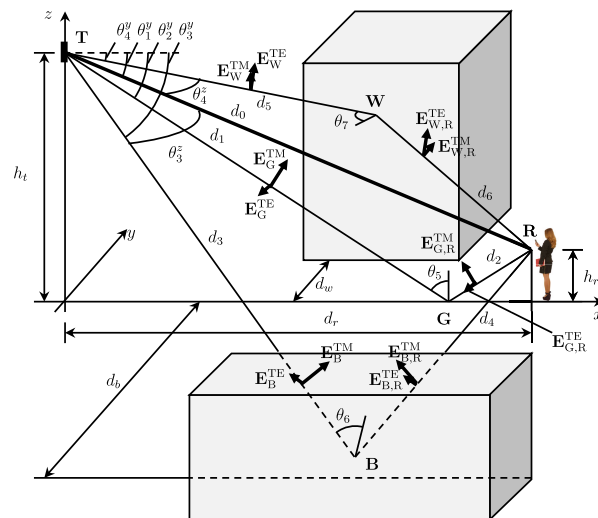

FIGURE 11. Four-path radio propagation used to generate the channels with polarization state used in Section IV.

V_x, V_y, and V_z may be either real-valued quantities (e.g., when they represent a position) or complex-valued quantities (e.g., when they represent electric field phasors). The dot product between $\mathbf{n}$ and $\mathbf{k}$ is denoted $\mathbf{n} \cdot \mathbf{k}$; the cross product between $\mathbf{n}$ and $\mathbf{k}$ is denoted $\mathbf{n} \times \mathbf{k}$.

The complex-valued electric field corresponding to transverse wave propagation at position $\mathbf{p}$ and at time t may be expressed as

$$\mathbf{E}(\mathbf{p}, t) = \mathbf{E}e^{j(\omega t - \mathbf{k} \cdot \mathbf{p})} \qquad (55)$$

where $\mathbf{E} = E_x\hat{\mathbf{x}} + E_y\hat{\mathbf{y}} + E_z\hat{\mathbf{z}}$ is a 3×1 vector denoting the (complex-valued) components of the electric field in the $\hat{\mathbf{x}}$, $\hat{\mathbf{y}}$, and $\hat{\mathbf{z}}$ directions; ω is the radian frequency (temporal period of the electric field); and $\mathbf{k} = k_x\hat{\mathbf{x}} + k_y\hat{\mathbf{y}} + k_z\hat{\mathbf{z}}$ is the wave vector that defines the direction of propagation. The magnitude of $\mathbf{k}$, $k \equiv |\mathbf{k}|$ is the wave number and may be expressed as $k = 2\pi/\lambda = 2\pi f/v_p$ where λ is the wavelength, v_p is the propagation velocity, and f is the frequency in cycles/s. For the purposes of this paper, (55) is written as the product of three components:

$$\mathbf{E}(\mathbf{p}, t) = \mathbf{E}e^{-j\mathbf{k} \cdot \mathbf{p}}e^{j\omega t}. \qquad (56)$$

The first term on the right-hand side of (56) quantifies the frequency-invariant magnitude, phase, and polarization state of the electric field. The second term on the right-hand side of (56) quantifies the frequency-dependent phase shift due to propagation delay. The third term on the right-hand side of (56) is the rotation operator. In the following, we are interested in the phasor terms $\mathbf{E}_p \equiv \mathbf{E}e^{-j\mathbf{k} \cdot \mathbf{p}}$ because this term defines the Fourier transform of the complex-valued low-pass equivalent channel in the three spatial dimensions.

A simple four-path propagation scenario corresponding to a downlink in an urban setting is illustrated in Figure 11. The basestation transmitter, located at point $\mathbf{T}$ on the z-axis, is equipped with massive MIMO antennas and performs beamforming. A 30° beamwidth is assumed for the following

reasons. The mmWave propagation experiments reported in [11], [46]–[48] simulated the use of beamforming by using a horn antenna with 15 dBi gain and half-power azimuth and elevation beamwidths of 28.8° and 30°, respectively. The analyses in [49], [50] were based on a beamwidth of 30°. Narrower beamwidths are possible. For example, the 64-element (8×8) phased-array antennas described in [51], [52] produce a beam at 28 GHz with a beamwidth of 11.5°.

The vertically-polarized beam is pointed at the pedestrian with a hand-held smartphone located at point **R**. The vertically-polarized 30° beamwidth illuminates the reflectors located at points **B**, **G**, and **W** shown in Figure 11. The four propagation paths are described as follows.

1) Line-of-sight propagation is assumed along the line **TR**. The departure angle from **T** is θ_1^y, measured in the $x-z$ plane (i.e., θ_1^y is a rotation about the y-axis), and θ_1^z measured in the $x-y$ plane (i.e., θ_1^z is a rotation about the z-axis).

2) A ground reflection at point **G** along the line segments **TG** and **GR**. The departure angle from **T** is θ_2^y, measured in the $x-z$ plane (i.e., θ_2^y is a rotation about the y-axis), and θ_2^z, measured in the $x-y$ plane (i.e., θ_2^z is a rotation about the z-axis). The incident angle at point **G** is θ_5 and is measured in the **TGR** plane.

3) A reflection off the side of a building across the street from the pedestrian. The reflection occurs at point **B** along line segments **TB** and **BR**. The departure angle from **T** is θ_3^y (a rotation about the y-axis) followed by θ_3^z (a rotation about the z-axis). The incidence angle is θ_6 and is measured in the **TBR** plane.

4) A reflection off the side of a building on the same side of the street as the pedestrian. The reflection occurs at point **W** along line segments **TW** and **WR**. The departure angle from **T** is θ_4^y (a rotation about the y-axis) followed by θ_4^z (a rotation about the z-axis). The incidence angle is θ_7 and is measured in the **TWR** plane.

The use of perspective in Figure 11 hides the fact that $\theta_1^y = \theta_3^y = \theta_4^y$.

In the material below, the technique is illustrated for propagation from **T** to **R** via the four propagation paths shown in Figure 11. The relationship between the point **R** and the four pairs of co-located cross-polarized antenna elements is illustrated in Figure 4. The calculations must be re-evaluated for each of the four receiver points corresponding to the four antenna pairs.

The electric field components at point **R**, denoted $\mathbf{E}_R$, comprises four components: the electric field due to line-of-site propagation $\mathbf{E}_{L,R}$, the electric field due to the ground reflection $\mathbf{E}_{G,R}$, the electric field due to the reflection off the building $\mathbf{E}_{B,R}$, and the electric field due to the reflection off the wall $\mathbf{E}_{W,R}$. Consequently, $\mathbf{E}_R$ may be expressed as

$$\mathbf{E}_R = \mathbf{E}_{L,R} e^{-j2\pi f \, d_0/v_p} + \mathbf{E}_{G,R} e^{-j2\pi f \, (d_1+d_2)/v_p}$$
$$+ \mathbf{E}_{B,R} e^{-j2\pi f \, (d_3+d_4)/v_p} + \mathbf{E}_{W,R} e^{-j2\pi f \, (d_5+d_6)/v_p} \quad (57)$$

where the distances $d_0, \ldots, d_6$ are defined in Figure 11 and are computed using straight-forward applications of geometry. Assuming the transmit antenna is aligned with the $\hat{\mathbf{z}}$ axis, it can be shown, after considerable effort, that [53]

$$\mathbf{E}_{L,R} = \mathbf{R}_z(\theta_1^z)\mathbf{R}_y(\theta_1^y)\mathbf{E}_0 e^{j\phi_L} \quad (58)$$
$$\mathbf{E}_{G,R} = \mathbf{E}_{G,R}^{\text{TM}} + \mathbf{E}_{G,R}^{\text{TE}}, \quad (59)$$
$$\mathbf{E}_{B,R} = \mathbf{E}_{B,R}^{\text{TM}} + \mathbf{E}_{B,R}^{\text{TE}}, \quad (60)$$
$$\mathbf{E}_{W,R} = \mathbf{E}_{W,R}^{\text{TM}} + \mathbf{E}_{W,R}^{\text{TE}}, \quad (61)$$

where the superscript "TM" refers to the transverse magnetic field linear polarization state and "TE" refers to the transverse electric field linear polarization state, both with respect to the incident plane (i.e., the plane defined by the **T**, **R**, and the reflection point). The phasor representing TM propagation is orthogonal to the direction of propagation and lies in the plane of incidence. The phasor representing TE propagation is orthogonal to the direction of propagation is normal to the plane of incidence. The elements in $(58) - (61)$ are defined in the following.

In (58), $\mathbf{R}_z(\theta)$ is the rotation matrix about the z-axis and is given by (76) below; $\mathbf{R}_y(\theta)$ is the rotation matrix about the y-axis and is given by (75) below; ϕ_L is the initial phase of the line-of-sight component; and $\mathbf{E}_0$ is the polarization state of the transmit antenna. In the calculations below, we use

$$\mathbf{E}_0 = \hat{\mathbf{z}}. \quad (62)$$

In (59), $\mathbf{E}_{G,R}^{TM}$ and $\mathbf{E}_{G,R}^{TE}$ are computed as follows. The electric field at point **G** is $\mathbf{E}_G = \mathbf{R}_z(\theta_2^z)\mathbf{R}_y(\theta_2^y)\mathbf{E}_0 \, e^{j\phi_G}$ where ϕ_G is the initial phase of the component propagating along path **TG**. Because the reflection has different characteristics for the TM and TE modes, $\mathbf{E}_G$ must be decomposed into its TM and TE modes in the **TGR** plane. Using $\hat{\mathbf{k}}_1$ to denote the normal vector in the direction **TG** and $\hat{\mathbf{n}}_1$ to denote the normal vector for the plane **TGR**, the TM component of $\mathbf{E}_G$ in the **TGR** plane may be expressed as

$$\mathbf{E}_G^{TM} = \left[\mathbf{E}_G \cdot \left(\hat{\mathbf{n}}_1 \times \hat{\mathbf{k}}_1\right)\right]\left(\hat{\mathbf{n}}_1 \times \hat{\mathbf{k}}_1\right)$$
$$= E_{G,x}^{TM}\hat{\mathbf{x}} + E_{G,y}^{TM}\hat{\mathbf{y}} + E_{G,z}^{TM}\hat{\mathbf{z}}. \quad (63)$$

After the reflection at point **G**, the TM component of the electric field at point **R** in the **TGR** plane is

$$\mathbf{E}_{G,R}^{TM} = r_{1,\text{TM}}\left(-E_{G,x}^{TM}\hat{\mathbf{x}} + E_{G,y}^{TM}\hat{\mathbf{y}} + E_{G,z}^{TM}\hat{\mathbf{z}}\right) \quad (64)$$

where $r_{1,\text{TM}}$ is the TM mode reflection coefficient at point **G** in the **TGR** plane and the negative sign on the $\hat{\mathbf{x}}$ component quantifies the direction change due to the reflection. The TE component of the electric field in the **TGR** plane is

$$\mathbf{E}_G^{TE} = \left(\mathbf{E}_G \cdot \hat{\mathbf{n}}_1\right)\hat{\mathbf{n}}_1 = E_{G,x}^{TE}\hat{\mathbf{x}} + E_{G,y}^{TE}\hat{\mathbf{y}} + E_{G,z}^{TE}\hat{\mathbf{z}}. \quad (65)$$

After the reflection at point **G**, the TE component of the electric field at point **R** in the **TGR** plane is

$$\mathbf{E}_{G,R}^{TE} = r_{1,\text{TE}}\left(-E_{G,x}^{TE}\hat{\mathbf{x}} + E_{G,y}^{TE}\hat{\mathbf{y}} + E_{G,z}^{TE}\hat{\mathbf{z}}\right) \quad (66)$$

where $r_{1,TE}$ is the TE mode reflection coefficient at point **G** in the **TGR** plane and the negative sign on the $\hat{\mathbf{x}}$ component quantifies the direction change due to the reflection.

In (60), $\mathbf{E}_{B,R}^{TM}$ and $\mathbf{E}_{B,R}^{TE}$ are computed as follows. The electric field at point **B** is $\mathbf{E}_B = \mathbf{R}_z(\theta_3^z)\mathbf{R}_y(\theta_3^y)\mathbf{E}_0 \, e^{j\phi_B}$ where ϕ_B is the initial phase of the component propagating along path **TB** and $\mathbf{R}_z(\theta)$ is the rotation matrix about the z-axis given by (76) below. Using $\hat{\mathbf{k}}_2$ to denote the normal vector in the direction **TB** and $\hat{\mathbf{n}}_2$ to denote the normal vector for the plane **TBR**, the TM component of $\mathbf{E}_B$ in the **TBR** plane may be expressed as

$$\mathbf{E}_B^{TM} = \left[\mathbf{E}_B \cdot \left(\hat{\mathbf{n}}_2 \times \hat{\mathbf{k}}_2 \right) \right] \left(\hat{\mathbf{n}}_2 \times \hat{\mathbf{k}}_2 \right)$$
$$= E_{B,x}^{TM}\hat{\mathbf{x}} + E_{B,y}^{TM}\hat{\mathbf{y}} + E_{B,z}^{TM}\hat{\mathbf{z}}. \qquad (67)$$

After the reflection at point **B**, the TM component of the electric field at point **R** in the **TBR** plane is

$$\mathbf{E}_{B,R}^{TM} = r_{2,TM} \left(-E_{B,x}^{TM}\hat{\mathbf{x}} + E_{B,y}^{TM}\hat{\mathbf{y}} + E_{B,z}^{TM}\hat{\mathbf{z}} \right) \qquad (68)$$

where $r_{2,TM}$ is the TM mode reflection coefficient at point **B** in the **TBR** plane and the negative sign on the $\hat{\mathbf{x}}$ component quantifies the direction change due to the reflection. The TE component of the electric field in the **TBR** plane is

$$\mathbf{E}_B^{TE} = \left(\mathbf{E}_B \cdot \hat{\mathbf{n}}_2 \right) \hat{\mathbf{n}}_2 = E_{B,x}^{TE}\hat{\mathbf{x}} + E_{B,y}^{TE}\hat{\mathbf{y}} + E_{B,z}^{TE}\hat{\mathbf{z}}. \qquad (69)$$

After the reflection at point **B**, the TE component of the electric field at point **R** in the **TBR** plane is

$$\mathbf{E}_{B,R}^{TE} = r_{2,TE} \left(-E_{B,x}^{TE}\hat{\mathbf{x}} + E_{B,y}^{TE}\hat{\mathbf{y}} + E_{B,z}^{TE}\hat{\mathbf{z}} \right) \qquad (70)$$

where $r_{2,TE}$ is the TE mode reflection coefficient at point **B** in the **TBR** plane and the negative sign on the $\hat{\mathbf{x}}$ component quantifies the direction change due to the reflection.

In (61), $\mathbf{E}_{W,R}^{TM}$ and $\mathbf{E}_{W,R}^{TE}$ are computed as follows. The electric field at point **W** is $\mathbf{E}_W = \mathbf{R}_z(\theta_4^z)\mathbf{R}_y(\theta_4^y)\mathbf{E}_0 \, e^{j\phi_W}$ where ϕ_W is the initial phase of the component propagating along path **TW**. Using $\hat{\mathbf{k}}_3$ to denote the normal vector in the direction **TW** and $\hat{\mathbf{n}}_3$ to denote the normal vector for the plane **TWR**, the TM component of $\mathbf{E}_W$ in the **TWR** plane may be expressed as

$$\mathbf{E}_W^{TM} = \left[\mathbf{E}_W \cdot \left(\hat{\mathbf{n}}_3 \times \hat{\mathbf{k}}_3 \right) \right] \left(\hat{\mathbf{n}}_3 \times \hat{\mathbf{k}}_3 \right)$$
$$= E_{W,x}^{TM}\hat{\mathbf{x}} + E_{W,y}^{TM}\hat{\mathbf{y}} + E_{W,z}^{TM}\hat{\mathbf{z}}. \qquad (71)$$

After the reflection at point **W**, the TM component of the electric field at point **R** in the **TWR** plane is

$$\mathbf{E}_{W,R}^{TM} = r_{3,TM} \left(-E_{W,x}^{TM}\hat{\mathbf{x}} + E_{W,y}^{TM}\hat{\mathbf{y}} + E_{W,z}^{TM}\hat{\mathbf{z}} \right) \qquad (72)$$

where $r_{3,TM}$ is the TM mode reflection coefficient at point **W** in the **TWR** plane and the negative sign on the $\hat{\mathbf{x}}$ component quantifies the direction change due to the reflection. The TE component of the electric field in the **TWR** plane is

$$\mathbf{E}_W^{TE} = \left(\mathbf{E}_W \cdot \hat{\mathbf{n}}_3 \right) \hat{\mathbf{n}}_3 = E_{W,x}^{TE}\hat{\mathbf{x}} + E_{W,y}^{TE}\hat{\mathbf{y}} + E_{W,z}^{TE}\hat{\mathbf{z}}. \qquad (73)$$

After the reflection at point **W**, the TE component of the electric field at point **R** in the **TWR** plane is

$$\mathbf{E}_{B,R}^{TE} = r_{3,TE} \left(-E_{W,x}^{TE}\hat{\mathbf{x}} + E_{W,y}^{TE}\hat{\mathbf{y}} + E_{W,z}^{TE}\hat{\mathbf{z}} \right) \qquad (74)$$

where $r_{3,TE}$ is the TE mode reflection coefficient at point **W** in the **TWR** plane and the negative sign on the $\hat{\mathbf{x}}$ component quantifies the direction change due to the reflection.

In the previous four paragraphs, the following rotation matrices were used,

$$\mathbf{R}_y(\theta) = \begin{bmatrix} \cos(\theta) & 0 & \sin(\theta) \\ 0 & 1 & 0 \\ -\sin(\theta) & 0 & \cos(\theta) \end{bmatrix} \qquad (75)$$

$$\mathbf{R}_z(\theta) = \begin{bmatrix} \cos(\theta) & -\sin(\theta) & 0 \\ \sin(\theta) & \cos(\theta) & 0 \\ 0 & 0 & 1 \end{bmatrix}, \qquad (76)$$

and the following reflection coefficients were used:

$$r_{1,TM} = \frac{n_2 \cos(\theta_5) - n_1\sqrt{1 - (n_1/n_2)^2 \sin^2(\theta_5)}}{n_2 \cos(\theta_5) + n_1\sqrt{1 - (n_1/n_2)^2 \sin^2(\theta_5)}} \qquad (77)$$

$$r_{1,TE} = \frac{n_1 \cos(\theta_5) - n_2\sqrt{1 - (n_1/n_2)^2 \sin^2(\theta_5)}}{n_1 \cos(\theta_5) + n_2\sqrt{1 - (n_1/n_2)^2 \sin^2(\theta_5)}} \qquad (78)$$

$$r_{2,TM} = \frac{n_2 \cos(\theta_6) - n_1\sqrt{1 - (n_1/n_2)^2 \sin^2(\theta_6)}}{n_2 \cos(\theta_6) + n_1\sqrt{1 - (n_1/n_2)^2 \sin^2(\theta_6)}} \qquad (79)$$

$$r_{2,TE} = \frac{n_1 \cos(\theta_6) - n_2\sqrt{1 - (n_1/n_2)^2 \sin^2(\theta_6)}}{n_1 \cos(\theta_6) + n_2\sqrt{1 - (n_1/n_2)^2 \sin^2(\theta_6)}} \qquad (80)$$

$$r_{3,TM} = \frac{n_2 \cos(\theta_7) - n_1\sqrt{1 - (n_1/n_2)^2 \sin^2(\theta_7)}}{n_2 \cos(\theta_7) + n_1\sqrt{1 - (n_1/n_2)^2 \sin^2(\theta_7)}} \qquad (81)$$

$$r_{3,TE} = \frac{n_1 \cos(\theta_7) - n_2\sqrt{1 - (n_1/n_2)^2 \sin^2(\theta_7)}}{n_1 \cos(\theta_7) + n_2\sqrt{1 - (n_1/n_2)^2 \sin^2(\theta_7)}}, \qquad (82)$$

where $n_1 = 1.000293$ is the refractive index of the propagation medium (air) and n_2 is the refractive index of the reflection surface.

The calculations were performed using the following values:

$$h_t = 30 \text{ m}$$
$$h_r = 1.15 \text{ m}$$
$$d_r = 230 \text{ m}$$
$$d_b = 15 \text{ m}$$
$$d_w = 2 \text{ m}$$
$$v_p = c/n_1 \text{ m/s}$$
$$n_2 = 2.2443 - j0.0597 \qquad (83)$$

where n_2 is the refractive index of concrete at 28 GHz [54]. The general form of the electric field at $\mathbf{R}^{(i,i+1)}$ is given by (84) on the top of the next page. This equation is interpreted as the Fourier-domain transfer function for three LTI systems,

$$
\begin{aligned}
\mathbf{E}_{\mathrm{R}^{(i,i+1)}} =\ & \left[c_{x,0}^{(i,i+1)} e^{-j2\pi f \tau_0} + c_{x,1}^{(i,i+1)} e^{-j2\pi f \tau_1} + c_{x,2}^{(i,i+1)} e^{-j2\pi f \tau_2} + c_{x,3}^{(i,i+1)} e^{-j2\pi f \tau_3} \right] \hat{\mathbf{x}} \\
& + \left[c_{y,0}^{(i,i+1)} e^{-j2\pi f \tau_0} + c_{y,1}^{(i,i+1)} e^{-j2\pi f \tau_1} c_{y,2}^{(i,i+1)} e^{-j2\pi f \tau_2} + c_{y,3}^{(i,i+1)} e^{-j2\pi f \tau_3} \right] \hat{\mathbf{y}} \\
& + \left[c_{z,0}^{(i,i+1)} e^{-j2\pi f \tau_0} + c_{z,1}^{(i,i+1)} e^{-j2\pi f \tau_1} + c_{z,2}^{(i,i+1)} e^{-j2\pi f \tau_2} + c_{z,3}^{(i,i+1)} e^{-j2\pi f \tau_3} \right] \hat{\mathbf{z}}
\end{aligned}
\tag{84}
$$

one for each spatial dimension. The corresponding impulse response is given by (42) and (43) in the main body. The values for each channel component at each of the four antenna-pair locations are given by (44) – (47).

Note that ''$1/R^2$'' spreading loss is not included in this analysis. In this sense the impulse response has a normalized amplitude. The spreading loss only influences the signal-to-noise ratio.

Close examination of (42), (43), and (44) – (47) shows that $\mathbf{E}_{\mathrm{L},R}$ and $\mathbf{E}_{\mathrm{G},R}$ have almost all of their energy in the $\hat{\mathbf{x}}$ and $\hat{\mathbf{z}}$ components. In contrast $\mathbf{E}_{\mathrm{B},R}$ and $\mathbf{E}_{\mathrm{W},R}$ have components in all three directions. Thus, the contribution in $\hat{\mathbf{y}}$ are due to $\mathbf{E}_{\mathrm{B},R}$ and $\mathbf{E}_{\mathrm{W},R}$. The conclusion is that if there were no reflection from the building and wall, the electric field components in $\hat{\mathbf{x}}$ and $\hat{\mathbf{z}}$ would be scaled versions of each other because all the electric field interactions would occur in the $x - z$ plane. Thus, the **TBR** and **TWR** propagation paths contribute to the $\hat{\mathbf{y}}$ component. It is the inclusion of these paths that creates impulse responses that are different in the $\hat{\mathbf{x}}$, $\hat{\mathbf{y}}$, and $\hat{\mathbf{z}}$ directions. Consequently, it is the reflections that occur *outside* the **TGR** plane that create the opportunity for polarization diversity gains.

REFERENCES

[1] (Oct. 2017). *IEEE 5G and Beyond Technology Roadmap White Paper*. [Online]. Available: https://5g.ieee.org/images/files/pdf/ieee-5g-roadmap-white-paper.pdf

[2] J. Proakis and M. Salehi, *Digital Communications*, 5th ed. New York, NY, USA: McGraw-Hill, 2007.

[3] M. Li, Z. Xu, Y. Ban, and Q. Yang, "Eight-port dual polarized MIMO antenna for 5G smartphone applications," in *Proc. IEEE Asia Pacific Conf. Antennas Propag.*, Kaohsiung, Taiwan, Jul. 2016, pp.195–196.

[4] A. Molisch, *Wireless Communications*, 2nd ed. West Sussex, U.K.: Wiley, 2011.

[5] W. Lee and Y. Yeh, "Polarization diversity for mobile radio," *IEEE Trans. Commun.*, vol. C-20, no. 5, pp. 913–923, Oct. 1972.

[6] R. G. Vaughan, "Polarization diversity in mobile communications," *IEEE Trans. Veh. Technol.*, vol. 39, no. 3, pp. 177–186, Aug. 1990.

[7] J. Jootar, J.-F. Diouris, and J. R. Zeidler, "Performance of polarization diversity in correlated Nakagami-m fading channels," *IEEE Trans. Veh. Technol.*, vol. 55, no. 1, pp. 128–136, Jan. 2006.

[8] A. Mchbal, N. A. Touhami, H. Elftouh, M. Moubadir, and A. Dkiouak, "Spatial and polarization diversity performance analysis of a compact MIMO antenna," *Procedia Manuf.*, vol. 32, pp. 647–652, 2019.

[9] K. Scott, E. B. Olasz, and A. Sendyk, "Diversity combining with MLSE equalisation," *IEE Proc. Commun.*, vol. 145, no. 2, pp. 105–108, 1998.

[10] P. Balaban and J. Salz, "Optimum diversity combining and equalization in digital data transmission with applications to cellular mobile radio. I. Theoretical considerations," *IEEE Trans. Commun.*, vol. 40, no. 5, pp. 885–894, May 1992.

[11] T. S. Rappaport, S. Sun, R. Mayzus, H. Zhao, Y. Azar, K. Wang, G. N. Wong, J. K. Schulz, M. Samimi, and F. Gutierrez, "Millimeter wave mobile communications for 5G cellular: It will work!" *IEEE Access*, vol. 1, pp. 335–349, May 2013.

[12] T. Rappaport, R. Heath, R. Daniels, and J. Murdock, *Millimeter Wave Wireless Communication*. Upper Saddle River, NJ, USA: Prentice-Hall, 2015.

[13] A. Alkhateeb and R. W. Heath, Jr., "Frequency selective hybrid precoding for limited feedback millimeter wave systems," *IEEE Trans. Commun.*, vol. 64, no. 5, pp. 1801–1818, May 2016.

[14] K. Venugopal, A. Alkhateeb, N. Gonzalez Prelcic, and R. W. Heath, Jr., "Channel estimation for hybrid architecture-based wideband millimeter wave systems," *IEEE J. Sel. Areas Commun.*, vol. 35, no. 9, pp. 1996–2009, Sep. 2017.

[15] K. Venugopal, N. Gonzalez-Prelcic, and R. W. Heath, Jr., "Optimal frequency-flat precoding for frequency-selective millimeter wave channels," *IEEE Trans. Wireless Commun.*, vol. 18, no. 11, pp. 5098–5112, Nov. 2019.

[16] Z. Gao, C. Hu, L. Dai, and Z. Wang, "Channel estimation for millimeter-wave massive MIMO with hybrid precoding over frequency-selective fading channels," *IEEE Commun. Lett.*, vol. 20, no. 6, pp. 1259–1262, Jun. 2016.

[17] J. Rodriguez-Fernandez, N. Gonzalez-Prelcic, K. Venugopal, and R. W. Heath, Jr., "Frequency-domain compressive channel estimation for frequency-selective hybrid millimeter wave MIMO systems," *IEEE Trans. Wireless Commun.*, vol. 17, no. 5, pp. 2946–2960, May 2018.

[18] J. Rodríguez-Fernández and N. González-Prelcic, "Channel estimation for frequency-selective mmWave MIMO systems with beam-squint," in *Proc. IEEE Global Commun. Conf. (GLOBECOM)*, Abu Dhabi, United Arab Emirates, Dec. 2018, pp. 1–6.

[19] M. Mohammadkarimi and M. Ardakani, "Optimal channel equalizer for mmWave massive MIMO using 1-bit ADCs in frequency-selective channels," *IEEE Commun. Lett.*, vol. 24, no. 4, pp. 882–885, Apr. 2020.

[20] W. Feng, Y. Wang, D. Lin, N. Ge, J. Lu, and S. Li, "When mmWave communications meet network densification: A scalable interference coordination perspective," *IEEE J. Sel. Areas Commun.*, vol. 35, no. 7, pp. 1459–1471, Jul. 2017.

[21] A. K. Gupta, J. G. Andrews, and R. W. Heath, Jr., "Impact of correlation between link blockages on macro-diversity gains in mmWave networks," in *Proc. IEEE Int. Conf. Commun. Workshops (ICC Workshops)*, Kansas City, MO, USA, May 2018, pp. 1–6.

[22] T. Rappaport, *Wireless Communications: Principles and Practice*, 2nd ed. Upper Saddle River, NJ, USA: Prentice-Hall, 2002.

[23] G. Ungerboeck, "Adaptive maximum-likelihood receiver for carrier-modulated data-transmission systems," *IEEE Trans. Commun.*, vol. C-22, no. 5, pp. 624–636, May 1974.

[24] G. Forney, "Maximum-likelihood sequence estimation of digital sequences in the presence of intersymbol interference," *IEEE Trans. Inf. Theory*, vol. IT-18, no. 3, pp. 363–378, May 1972.

[25] E. McCune, "5G-NR bandwidth efficient modulation options for efficient link operation that are compatible with mmW transistor nonlinearities," in *Proc. IEEE 5G World Forum (5GWF)*, Santa Clara, CA, USA, Jul. 2018, pp. 289–293.

[26] T. Nitsche, *Directional 60 GHz Communication for Multi-Gigabit-Per-Second Wi-Fi*, Standard 802.11ad, Dec. 2014.

[27] S. Buzzi, C. D'Andrea, T. Foggi, A. Ugolini, and G. Colavolpe, "Single-carrier modulation versus OFDM for millimeter-wave wireless MIMO," *IEEE Trans. Commun.*, vol. 66, no. 3, pp. 1335–1348, Mar. 2018.

[28] H. Sari, G. Karam, and I. Jeanclaude, "Transmission techniques for digital terrestrial TV broadcasting," *IEEE Commun. Mag.*, vol. 33, no. 2, pp. 100–109, Feb. 1995.

[29] F. Arabian, M. Rice, and R. Q. Hu, "Who's on first in 5G mobile networks: Equalizers or polarization diversity combiners?" in *Proc. IEEE Inter-Mountain Eng., Technol., Comput. Conf.*, Orem, UT, USA, Oct. 2020, pp. 1–6.

[30] L. Lewin, "Diversity reception and automatic phase correction," *The Proc. Inst. Electr. Engineers*, vol. 109, no. 46, pp. 295–304, Jul. 1962.

[31] Q. Liu and Y. Wan, "A unified MLSE detection technique for TDMA digital cellular radio," in *Proc. IEEE Veh. Technol. Conf.*, Secaucus, NJ, USA, May 1993, pp. 265–268.

[32] X. Ma and W. Zhang, "Fundamental limits of linear equalizers: Diversity, capacity, and complexity, diversity, capacity, and complexity," *IEEE Trans. Inf. Theory*, vol. 54, no. 8, pp. 3442–3456, Aug. 2008.

[33] A. Tajer, A. Nosratinia, and N. Al-Dhahir, "Diversity analysis of symbol-by-symbol linear equalizers," *IEEE Trans. Commun.*, vol. 59, no. 9, pp. 2343–2348, Sep. 2011.

[34] S. H. Song and K. B. Letaief, "Diversity analysis for linear equalizers over ISI channels," *IEEE Trans. Commun.*, vol. 59, no. 9, pp. 2414–2423, Sep. 2011.

[35] A. Hedayat, A. Nosratinia, and N. Al-Dhahir, "Outage probability and diversity order of linear equalizers in frequency-selective fading channels," in *Proc. 28th Asilomar Conf. Signals, Syst. Comput.*, Pacific Grove, CA, USA, Nov. 2004, pp. 7–10.

[36] J. Chen and T. Pratt, "Three-dimensional geometry-based stochastic modeling and performance and 4×4 space-polarized mobile-to-mobile wideband MIMO channels," in *Proc. IEEE Global Commun. Conf.*, Atlanta, GA, USA, Dec. 2013, pp. 3936–3941.

[37] M. Ilic and M. Pejanovic-Djurisic, "SER performance of OFDM polarization diversity system with EGC," in *Proc. IEEE Int. Conf. Wireless Mobile Comput., Netw. Commun.*, Avignon, France, Oct. 2008, pp. 12–14.

[38] J. Lempiäinen, J. Laiho-Steffens, and S. Wacker, "Experimental results of cross polarization discrimination and signal correlation values for a polarization diversity scheme," in *Proc. IEEE Veh. Technol. Conf.*, Phoenix, AZ, USA, May 1997, pp. 1498–1502.

[39] J. J. A. Lempiainen and J. K. Laiho-Steffens, "The performance of polarization diversity schemes at a base station in small/micro cells at 1800 MHz," *IEEE Trans. Veh. Technol.*, vol. 47, no. 3, pp. 1087–1092, Aug. 1998.

[40] P. Soma, D. Baum, V. Erceg, R. Krihnamoorthy, and S. Paulraj, "Analysis and modeling of multiple-input multiple-output (MIMO) radio channel based on outdoor measurements conducted at 2.5 GHz for fixed BWA applications," in *Proc. IEEE Int. Conf. Commun.*, New York, NY, USA, Apr./May 2002, pp. 272–276.

[41] T. G. Pratt, R. Srinivasan, and S. Nguyen, "Input-to-output cross polarization discrimination (IOXPD) dispersion model for mobile-to-mobile LOS wireless communications MIMO channels," in *Proc. Wireless Telecommunications Symp.*, Pomona, CA, USA, Apr. 2008, pp. 24–26.

[42] F. Talebi and T. Pratt, "Bounding the ergodic capacity of asymmetric 2×2 dual-polarized channels," in *Proc. IEEE Mil. Commun. Conf.*, Orlando, FL, USA, Oct./Nov. 2012, pp. 1–6.

[43] F. Talebi and T. Pratt, "Approximating the outage capacity of asymmetric 2×2 dual-polarized MIMO at high SNR," in *Proc. IEEE Int. Conf. Comput., Netw. Commun.*, San Diego, CA, USA, Jan. 2013, pp. 290–294.

[44] J. Chen and T. Pratt, "Diversity measure of co-polarized and polarized MIMO architectures over wideband mobile-to-mobile channels," in *Proc. IEEE Mil. Commun. Conf.*, San Diego, CA, USA, Nov. 2013, pp. 1262–1267.

[45] M. Ivrlac and J. Nossek, "Quantifying diversity and correlation in Rayleigh fading MIMO communication systems," in *Proc. IEEE Int. Symp. Signal Process. Inf. Technol.*, Darmstadt, Germany, Dec. 2003, pp. 158–161.

[46] S. Rajagopal, S. Abu-Surra, and M. Malmirchegini, "Channel feasibility for outdoor non-line-of-sight mmWave mobile communication," in *Proc. IEEE Veh. Technol. Conf.*, Quebéc City, MA, Canada, Sep. 2012, pp. 1–6.

[47] M. K. Samimi, G. R. MacCartney, S. Sun, and T. S. Rappaport, "28 GHz millimeter-wave ultrawideband small-scale fading models in wireless channels," in *Proc. IEEE Veh. Technol. Conf. (VTC Spring)*, Nanjing, China, May 2016, pp. 1–6.

[48] M. K. Samimi, S. Sun, and T. S. Rappaport, "MIMO channel modeling and capacity analysis for 5G millimeter-wave wireless systems," in *Proc. 10th IEEE Eur. Conf. Antennas Propag. (EuCAP)*, Davos, Switzerland, Apr. 2016, pp. 1–5.

[49] T. Bai and R. W. Heath, Jr., "Coverage and rate analysis for millimeter-wave cellular networks," *IEEE Trans. Wireless Commun.*, vol. 14, no. 2, pp. 1100–1114, Feb. 2015.

[50] A. T. Nassar, A. I. Sulyman, and A. Alsanie, "Radio capacity estimation for millimeter wave 5G cellular networks using narrow beamwidth antennas at the base stations," *Int. J. Antennas Propag.*, vol. 2015, pp. 1–6, Oct. 2015, doi: 10.1155/2015/878614.

[51] M. Ishfaq, T. Rahman, Y. Yamada, and K. Sakakibara, "8×8 phased series fed patch antenna array at 28 GHz for 5G mobile base station antennas," in *Proc. IEEE-APS Topical Conf. Antennas Propag. Wireless Commun. (APWC)*, Verona, Italy, Sep. 2017, pp. 160–162.

[52] R. Valkonen, "Compact 28-GHz phased array antenna for 5G access," in *IEEE MTT-S Int. Microw. Symp. Dig.*, Philadelphia, PA, Jun. 2018, pp. 1334–1337.

[53] C. Balanis, *Advanced Engineering Electromagnetics*. Hoboken, NJ, USA: Wiley, 1989.

[54] M. Samimi and T. Rappaport, "Characterization of the 28 GHz millimeter-wave dense urban channel for future 5G mobile cellular," NYU Polytech. School Eng., Brooklyn, NY, USA, Tech. Rep. 2014-001, Jun. 2014.

FARAH ARABIAN (Student Member, IEEE) received the B.Sc. degree in electrical engineering from the Sadjad University of Technology, Mashhad, Iran, in 2010, and the M.Sc. degree in communications engineering from the Amirkabir University of Technology, Tehran, Iran, in 2013. She is currently pursuing the Ph.D. degree in electrical engineering with Brigham Young University.

She worked with Huawei and Nokia as a UMTS/LTE RF Planning and Optimization Engineer, from 2014 to 2016, and from 2016 to 2017. Her research interests include 5G cellular networks, digital communication theory, and signal processing.

GREGORY P. NORDIN (Senior Member, IEEE) received the Ph.D. degree in electrical engineering from the University of Southern California, in 1992.

From 1984 to 1992, he worked with Hughes Aircraft Company, the last three years of which were at the Hughes Research Laboratories, Malibu, CA, USA. From 1992 to 2005, he was with the Electrical and Computer Engineering Department, The University of Alabama, Huntsville, AL, USA, where he was a Founding Director of the University's Nano and Micro Devices Center. He joined the Electrical and Computer Engineering Department, Brigham Young University, as a Professor, in 2005. His research interests include 3D printing for microfluidics, and micro- and nano-fabricated devices for biosensing, photonics, and MEMS.

MICHAEL RICE (Fellow, IEEE) received the Ph.D. degree from Georgia Tech, Atlanta, GA, USA, in 1991. He was with Digital Transmission Systems Inc., Atlanta. He joined the Faculty of Brigham Young University, Provo, UT, USA, in 1991, where he is currently a Professor with the Department of Electrical and Computer Engineering. From 1994 to 1995, he was a NASA/ASEE Summer Faculty Fellow with the Jet Propulsion Laboratory, Pasadena, CA, USA, where he worked on land mobile satellite systems. From 1999 to 2000, he was a Visiting Scholar with the Communication Systems and Signal Processing Institute, San Diego State University. He has been a Consultant to both Government and Industry on telemetry related issues. His research interests include digital communication theory and statistical signal processing with a special emphasis on applications to aeronautical telemetry and software radio design. He is a member of the IEEE Communications Society. He is the Past Chair of the Communication Theory Technical Committee. He is also a member of the Aerospace and Electronic Systems Society. He currently serves as an Associate Member of the Telemetry Group of the Range Commander's Council. He is the Editor-in-Chief of the IEEE TRANSACTIONS ON AEROSPACE AND ELECTRONIC SYSTEMS. He is currently serving on the Board of Governors for the Aerospace and Electronic Systems Society.

• • •